# REPORT DOCUMENTATION PAGE

*Form Approved*
*OMB No. 0704-0188*

Public reporting burden for this collection of information is estimated to average 1 hour per response, including the time for reviewing instructions, searching existing data sources, gathering and maintaining the data needed, and completing and reviewing the collection of information. Send comments regarding this burden estimate or any other aspect of this collection of information, including suggestions for reducing this burden, to Washington Headquarters Services, Directorate for Information Operations and Reports, 1215 Jefferson Davis Highway, Suite 1204, Arlington, VA 22202-4302, and to the Office of Management and Budget, Paperwork Reduction Project (0704-0188), Washington, DC 20503.

**1. AGENCY USE ONLY** *(Leave blank)*

**2. REPORT DATE**
15.Oct.99

**3. REPORT TYPE AND DATES COVERED**
THESIS

**4. TITLE AND SUBTITLE**
DC MAGNETRON REACTIVE SPUTTERING OF LOW STRESS A1N PIEZOELECTRIC THIN FILMS FOR MEMS APPLICATION

**5. FUNDING NUMBERS**

**6. AUTHOR(S)**
2D LT HSIEH PETER Y

**7. PERFORMING ORGANIZATION NAME(S) AND ADDRESS(ES)**
MASSACHUSETTS INSTITUTE OF TECHNOLOGY

**8. PERFORMING ORGANIZATION REPORT NUMBER**

**9. SPONSORING/MONITORING AGENCY NAME(S) AND ADDRESS(ES)**
THE DEPARTMENT OF THE AIR FORCE
AFIT/CIA, BLDG 125
2950 P STREET
WPAFB OH 45433

**10. SPONSORING/MONITORING AGENCY REPORT NUMBER**
FY99-301

**11. SUPPLEMENTARY NOTES**

**12a. DISTRIBUTION AVAILABILITY STATEMENT**
Unlimited distribution
In Accordance With AFI 35-205/AFIT Sup 1

**DISTRIBUTION STATEMENT A**
**Approved for Public Release**
**Distribution Unlimited**

**12b. DISTRIBUTION CODE**

**13. ABSTRACT** *(Maximum 200 words)*

19991108 134

**14. SUBJECT TERMS**

**15. NUMBER OF PAGES**
52

**16. PRICE CODE**

**17. SECURITY CLASSIFICATION OF REPORT**

**18. SECURITY CLASSIFICATION OF THIS PAGE**

**19. SECURITY CLASSIFICATION OF ABSTRACT**

**20. LIMITATION OF ABSTRACT**

DTIC QUALITY INSPECTED 4

# DC Magnetron Reactive Sputtering of Low Stress AlN Piezoelectric Thin Films for MEMS Application

by

Peter Y. Hsieh

B.S. Materials Science and Biology
United States Air Force Academy, 1997

SUBMITTED TO THE DEPARTMENT OF MATERIALS SCIENCE AND ENGINEERING
IN PARTIAL FULFILLMENT OF THE REQUIREMENTS FOR THE DEGREE OF

MASTER OF SCIENCE IN MATERIALS SCIENCE AND ENGINEERING
AT THE
MASSACHUSETTS INSTITUTE OF TECHNOLOGY

FEBRUARY 1999

Copyright © 1999 Peter Y. Hsieh. All rights reserved.

The author hereby grants to MIT and the Charles Stark Draper Laboratory
permission to reproduce and to distribute publicly
paper and electronic copies of this thesis document in whole or in part.

Signature of Author: _____
Department of Materials Science and Engineering
January 15, 1999

Approved by: _____
Dr. Kaplesh Kumar
Technical Supervisor, Charles Stark Draper Laboratory

Certified by: _____
Rafael Reif
Professor of Electrical Engineering, Thesis Supervisor

Certified by: _____
Eugene A. Fitzgerald
Professor of Materials Science and Engineering, Thesis Reader

Accepted by: _____
Linn W. Hobbs
John F. Elliott Professor of Materials
Chairman, Department Committee on Graduate Students

This page left intentionally blank.

# DC Magnetron Reactive Sputtering of Low Stress AlN Piezoelectric Thin Films for MEMS Application

by

Peter Y. Hsieh

Submitted to the Department of Materials Science and Engineering
on January 15, 1999, in Partial Fulfillment of the
Requirements for the Degree of Master of Science in
Materials Science and Engineering

ABSTRACT

Microelectromechanical systems (MEMS) often incorporate piezoelectric thin films to actuate and detect motion of mechanical structures. Aluminum nitride is advantageous for MEMS use because it can be deposited at low temperatures, is easily patterned using conventional photolithographic techniques, and is compatible with CMOS contaminant requirements for silicon IC foundries. In this work, AlN thin films were deposited on silicon for use in a MEMS ultrasonic resonator. The resonator is configured as a gravimetric chemical sensor. A rotatable central composite designed experiment was performed to optimize film properties affecting device performance: film crystallinity, stress, and uniformity. Film property response characterization was conducted with x-ray diffractometry, spectroscopic ellipsometry, and surface profilometry. Optimization of film deposition parameters improved AlN film properties in the MEMS sensors.

Film property characterization using response surface methodology indicated microstructural changes due to sputtered particle bombardment of the growing film surface. Surface morphology of the sputtered AlN films was assessed using tapping mode atomic force microscopy and scanning electron microscopy. Energetic particle bombardment of the growing film surface helped to yield dense crystalline films with zone T microstructure. Thermalization of the impinging particle flux resulted in voided films with zone 1 microstructure with inferior film properties.

Correlation between film crystallinity and oxygen content was explored with x-ray photoelectron spectrometry. Changes in film microstructure and composition are correlated with variations in deposition parameters. Adatom mobility during film growth appears to play an important role in determining final film properties.

Thesis Supervisor: Rafael Reif
Title: Professor, Department of Electrical Engineering and Computer Science
Director, Microsystems Technology Laboratory

This page left intentionally blank.

TABLE OF CONTENTS


| | Page |
|---|---|
| ABSTRACT | 3 |
| TABLE OF CONTENTS | 5 |
| LIST OF ILLUSTRATIONS AND FIGURES | 7 |
| LIST OF TABLES | 8 |
| ACKNOWLEDGMENTS | 9 |
| 1. INTRODUCTION | |
| 1.1 Piezoelectric thin films | 11 |
| 1.2 Objectives | 12 |
| 2. THEORY AND LITERATURE REVIEW | |
| 2.1 AlN deposition techniques | 13 |
| 2.2 Glow discharge structure | 15 |
| 2.3 Particle flux energy | 17 |
| 2.4 Particle flux population | 19 |
| 2.5 Adatom mobility and surface nucleation | 20 |
| 2.6 Film growth and modification | 23 |
| 2.7 Film microstructure and properties | 25 |
| 3. EXPERIMENTAL | |
| 3.1 Design | 28 |
| 3.2 Apparatus | 31 |
| 3.3 Deposition protocol | 32 |
| 3.4 Film analysis | 33 |
| 3.5 Potential sources of error | 34 |
| 4. RESULTS AND DISCUSSION | |
| 4.1 Property response surface | 36 |
| 4.1.1 *Crystallinity* | 36 |
| 4.1.2 *Stress* | 40 |
| 4.1.3 *Uniformity* | 42 |
| 4.2 Microstructure | 45 |
| 4.2.1 *Surface morphology* | 45 |
| 4.2.2 *Fracture morphology* | 48 |
| 4.2.3. *Grain size* | 48 |

4.3 Roughness 50
4.3.1 *Substrate* 50
4.3.2 *Growth* 51
4.4 Composition 52

5. CONCLUSION 53

6. FUTURE WORK 54

APPENDIX
A.1 Data summary 55
A.2 Residuals for response surface models 57
A.3 Standard error of response surfaces 58

BIBLIOGRAPHY 59

## LIST OF ILLUSTRATIONS AND FIGURES


| | | Page |
|---|---|---|
| Figure 1 | Packaged Draper Laboratory MEMS Flexural Plate Wave Chemical Sensors | 12 |
| Figure 2 | Glow Discharge Structure for Magnetron Sputtering | 15 |
| Figure 3 | Theoretical Flux Thermalization Distance | 18 |
| Figure 4 | Sputtered Particle Energy Distribution Profile | 18 |
| Figure 5 | Z1-ZT-Z2 Microstructures for DMT Zone Model | 22 |
| Figure 6 | Modified Perkin-Elmer 4410 DC Magnetron Sputtering System | 31 |
| Figure 7 | Electromechanical Coupling Coefficient ($K^2$) and Rocking Curve FWHM | 36 |
| Figure 8 | Normalized Peak Intensity and Rocking Curve FWHM | 37 |
| Figure 9 | Peak Intensity Response Surface | 38 |
| Figure 10 | Rocking Curve Response Surface | 39 |
| Figure 11 | Stress Response Surface | 42 |
| Figure 12 | Film Thickness Wafer Map | 43 |
| Figure 13 | Average Film Thickness as Function of Radial Distance for Study | 43 |
| Figure 14 | Device Wafer Output Magnitude Wafer Map | 44 |
| Figure 15 | AlN Surface Morphology as a Function of Deposition Power and Pressure | 46 |
| Figure 16 | Microstructural Zone Transitions due to Deposition Power and Pressure | 47 |
| Figure 17 | AlN Film Fracture Surface | 48 |
| Figure 18 | Film Crystallite Size and X-ray Peak Intensity | 49 |
| Figure 19 | Z1-ZT Transitional Film Surface | 52 |

## LIST OF TABLES


| | | Page |
|---|---|---|
| Table 1 | Theoretical and Measured Piezoelectric Constants of Selected Thin Film Materials | 11 |
| Table 2 | Al Diffusion Distance as a function of Substrate Temperature and Material | 22 |

ACKNOWLEDGMENTS

This thesis was prepared at the Charles Stark Draper Laboratory and the Microsystems Technology Laboratories with financial support from the Draper Laboratory Independent Research and Development Project Number 900: "Characterization of AlN Thin Films for Micromachined Devices" (CSDL DL-H-505342). Analysis of deposited films utilized the MRSEC Shared Facilities supported by the National Science Foundation under award number DMR-9400334.

The author gratefully acknowledges the assistance of Dr. Brian Cunningham in providing device data and insights pertinent to the findings presented in this work.

Publication of this thesis does not constitute approval by Draper or MTL of the findings or conclusions contained herein. It is published for the exchange and stimulation of ideas.

Permission is hereby granted by the author to the Massachusetts Institute of Technology to reproduce any or all of this thesis.

This page left intentionally blank.

## 1. INTRODUCTION

Thin film materials processing is an integral part of the semiconductor industry. The miniaturization of integrated circuit components has continuously reduced the cost and increased the capabilities of microelectronic circuits. The development of microelectromechanical systems (MEMS) extends the scope of component miniaturization to analog devices. MEMS sensors and actuators are fabricated using bulk and surface micromachining techniques initially developed for microelectronic circuits. Devices based on MEMS technology offer both economy of scale in production and potential for novel engineering applications due to their decreased size and weight.

### 1.1 Piezoelectric thin films

The expanding scope of MEMS applications places increasing demands on the underlying materials technology. Issues of peripheral interest in electronics processing may be central in the design and fabrication of MEMS devices. One such issue is the low temperature deposition of piezoelectric thin films. Many MEMS devices utilize piezoelectric thin films to actuate and detect the motion of mechanical structures. Mechanical stress and strain are coupled with electric intensity and displacement fields in piezoelectric films, providing a direct and efficient method for the conversion of mechanical forces to electrical signals.[1] The central role of piezoelectric materials in transducing signals and forces provides an impetus to improve the current understanding of piezoelectric materials and film processing issues in MEMS fabrication

Numerous piezoelectric materials, ranging from ceramics to polymers, have been identified for use in electromechanical systems.[2] Materials investigated for MEMS applications include ZnO, AlN, and $Pb(Zr_xTi_{1-x}O_3)$.[3] PZT has a significantly higher piezoelectric coefficient compared to ZnO and AlN (Table 1). However, deposition of PZT thin films require high processing temperatures which may cause interdiffusion and delamination.[3] In addition, control of composition and structure can prove problematic for multicomponent films. Binary films

| | ZnO | CdS | CdSe | PZT | AlN |
|---|---|---|---|---|---|
| $d_{33}$ [$10^{-12}$ C/N] (calculated)[2] | 12.4 | 10.3 | 7.8 | 268 | 5 |
| $d_{33}$ (measured)[3] | 7.4 | | | 98 | 3.9 |
| $d_{31}$ (calculated)[2] | -5.0 | -5.2 | -3.9 | | |

**Table 1**: Theoretical and Measured Piezoelectric Constants of Selected Thin Film Materials[2,3]

such as ZnO and AlN can be deposited at lower substrate temperatures while maintaining desired film properties. Though ZnO thin films are frequently utilized in the fabrication of MEMS devices,[2] Zn is incompatible with CMOS requirements. Trace Zn causes haze formation and decreases minority carrier lifetime in Si.[4] AlN is an alternative piezoelectric material that offers several advantageous qualities. AlN has the highest surface acoustic wave (SAW) velocity of all known piezoelectric materials, a property of interest in the fabrication of MEMS ultrasonic resonators.[5] Low temperature deposition of AlN yields chemically stable films with piezoelectric coupling coefficients similar in magnitude to ZnO. The material is CMOS compatible, a key consideration for on-chip integration of electronics with MEMS devices.

## 1.2 Objectives

This work demonstrates the use of AlN in a MEMS ultrasonic resonator configured as a chemical sensor (Figure 1) and explores material processing issues affecting film quality and device performance. More specifically, it seeks to optimize deposition conditions for AlN thin films used in device fabrication. The objectives of this thesis are to:

1. Characterize film properties and microstructure with respect to deposition parameters in DC magnetron reactive sputtered AlN thin films.
2. Identify key parameters affecting film crystallinity, stress, and thickness uniformity and relate the parameters to underlying physical processes.
3. Optimize film deposition parameters for device processing based on empirical results.

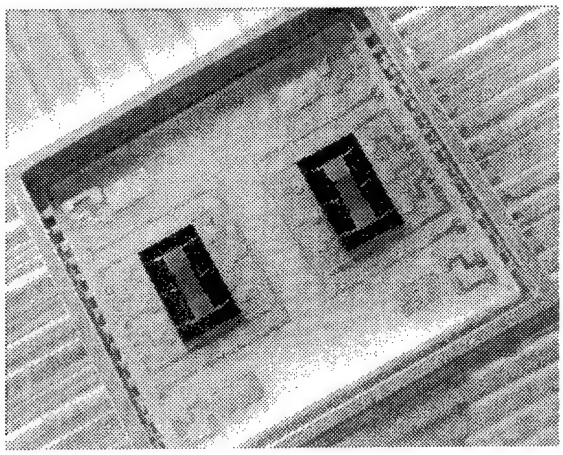

**Figure 1**: Packaged Draper Laboratory MEMS Flexural Plate Wave Chemical Sensors

## 2. Theory and Literature Review

### 2.1 AlN deposition techniques

Aluminum nitride is a wide bandgap semiconductor ($E_g$=6.02eV) with a high melting point (in excess of 2200°C under nitrogen atmosphere).[6] In the presence of oxygen, AlN oxidizes to form $Al_2O_3$ and $N_2$. However, the rate of reaction is not appreciable under 850°C.[7] The high melting point and affinity for oxygen constrain deposition and postdeposition processing conditions (section 2.4). Nevertheless, various techniques have been used successfully to deposit AlN thin films. Sputtering and chemical vapor deposition techniques are prevalent for most applications, though energy beam based techniques have also been demonstrated. While each technique has its strengths and weaknesses, sputtering is preferable for low temperature deposition and MEMS applications.

Sputtering is a physical deposition process which uses ions generated in a glow discharge plasma to physically eject atoms from the target. The ions are accelerated toward the target surface by an electric field. Collision between the accelerated ions and the target surface initiates a series of phonon interactions within the target. This may lead to the ejection of target atoms from the surface through momentum transfer. Concurrently, the impact generates secondary electrons that help to sustain the glow discharge. The sputtering process is energetically inefficient, with only 1% of the incident ion energy present in the ejected target atoms.[8]

Several modes of operation are commonly encountered in sputtering. Direct current sputtering (DC) is typically used for conductive targets, while radio frequency (RF) sputtering is used for insulating targets. DC sputtering of a nonconductive surface rapidly results in surface charge buildup, which extinguishes the glow discharge (see section 2.2). RF sputtering circumvents the problem by using a rapidly oscillating electrical field (~10MHz) which neutralizes the charge buildup. Ions in the glow discharge are too massive to respond to the oscillating field, and behave as though the field is DC.

The ionization rate of glow discharge gases is dependent on the secondary electron density and glow discharge gas pressure. The minimum operating pressure of early diode sputtering systems ranged between 10-100 mtorr. Magnetron sputtering systems reduced the minimum operating pressure to 1-10 mtorr. The magnetic fields imposed by permanent magnets help to confine secondary electrons near the target surface. The resulting increase in

electron density improves the ionization rate, allowing for a lower operating pressure.

Insulating films such as AlN can be deposited using DC sputtering if the target surface is kept conductive. This can be accomplished via reactive sputtering, where a metallic target is sputtered in the presence of an activated glow discharge. Sputtered atoms react with glow discharge gases to form the target compound. The target surface is kept conductive if the rate of insulating film formation is less than the rate of film removal via sputtering. A sharp transition between the metallic mode and insulating mode occurs at the target surface if this is not the case, and removal of the insulating film layer becomes necessary.[9]

Early reports on RF reactive sputtering indicated that deposition on high temperature substrates (1100-1200°C) produced epitaxial AlN films.[10,11] Crystalline films deposited at low temperatures using RF and DC sputtering took longer to realize.[12,13,14] A number of subsequent papers sought to identify and explain film properties based on observed film microstructures. The experimental evidence supported the Movchan-Demchishin-Thornton zone model, which explain some of the observed changes in film property as deposition conditions are changed. However, existing models do not directly address changes in the piezoelectric response of sputtered AlN films as a function of the film microstructure and composition. An improved understanding of the relationship between film piezoelectricity and structure in sputtered films is clearly advantageous in the fabrication of MEMS devices for both DC and RF sputtering.

Chemical vapor deposition (CVD) utilizes chemical precursors that decompose to form AlN, typically on high temperature substrates. Plasma enhanced CVD (PECVD) and low pressure metal-organic CVD (LP-MOCVD) have been used to produce high quality epitaxial AlN thin films using lattice-matched substrates.[7,15] Films deposited via CVD techniques are typically superior to those deposited via other techniques with regards to film epitaxy. However, the high temperature used in most AlN CVD processes remains problematic for applications where residual thermal stress is an issue. Other AlN deposition methods have also been reported in the literature. Recent examples include plasma enhanced molecular beam epitaxy (PEMBE),[16,17] electron cyclotron resonance (ECR) dual ion beam sputtering,[18] and pulsed laser ablation.[19,20] Similarities and differences in resultant film structure and properties often serve to highlight underlying film nucleation and growth mechanisms at work during deposition. The topic will be explored in greater detail in subsequent sections.

Of the techniques available for AlN deposition, reactive sputtering compares favorably with the others for MEMS fabrication. Polycrystalline films can be deposited at low temperatures on a number of substrates, while maintaining c-axis orientation within grains and smooth film surfaces. Low deposition temperatures limit the magnitude of thermal stress resulting from mismatch in the substrate and film coefficients of thermal expansion. Sputtering is the predominant deposition technique used in VLSI/ULSI metallization.[21] Given the widespread availability of the established industrial base, reactive sputtering represents a promising approach for the large scale fabrication of MEMS devices incorporating piezoelectric AlN thin films.

## 2.2 Glow discharge structure

Even under ideal conditions, the glow discharge plasma environment is complex and difficult to model.[22] Reactive sputtering introduces reaction chemistry and additional physical factors, further complicating the issue. However, the utility of the technique in MEMS fabrication provides a strong incentive towards a better understanding of this environment to improve control over the resulting film properties.

The general structure of a glow discharge plasma comprises the cathode, Crookes dark space (cathode sheath), negative glow region, Faraday dark space, positive column, anode dark space, and anode (Figure 2).[21,23]

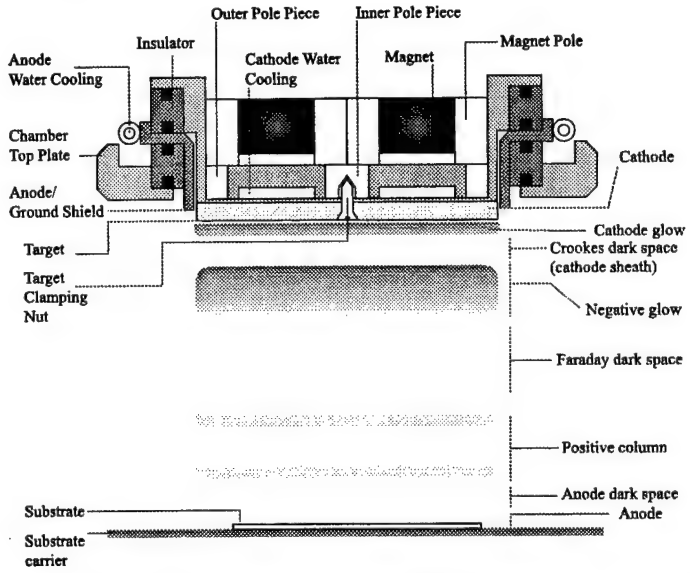


**Figure 2**: Glow Discharge Structure for Magnetron Sputtering

The cathode is made of the target material, typically a metal in the case of reactive sputtering. The surface of the cathode may be oxidized or nitrided to an unknown degree during sputtering, depending on the composition of the working gas. The emission of secondary electrons from the cathode surface is important in sustaining the glow discharge plasma.

The Crookes dark space, or cathode sheath, is a region where the electric potential rapidly increases. The sheath electric field accelerates electrons generated by ion bombardment away from the target surface and ionized gas particles from the glow discharge towards the target surface. The negative glow begins where the electrons have gained sufficient energy to begin ionizing the working gas particles. Impact ionization of the working gas by the impinging electrons gives rise to the characteristic glow as well as additional secondary electrons. Chemical activation of the working gas by electron bombardment plays a significant role in reactive sputtering.[9] Molecular nitrogen is stable and normally will not react with metallic aluminum. Electron bombardment of nitrogen working gas results in molecules in metastable states and atomic nitrogen, which are more reactive and will react with aluminum atoms.

The kinetic energy of sputtered target atoms and reflected fast neutral atoms begins to be diminished in the negative glow via collisions with gas particles. If the mean free path of the sputtered particles is sufficiently long, relatively few collisions occur and a majority of the particles strike the substrate surface with much of their initial momentum. A short mean free path results in numerous thermalizing collisions with working gas particles. Thermalized atoms lose their initial momentum, resulting in a more diffusion-based deposition process.[24,25]

The normalized translational energy distribution of the sputtered particles is given by

$$\frac{dN/dE_t}{N} = \frac{2E_b E_t}{(E_t + E_b)^3} \qquad (1)$$

$E_t$ = Translational kinetic energy (eV),
$E_b$ = Surface binding energy (eV)

The mean free path ($\lambda$) for the sputtered particles is

$$\lambda = \frac{\sqrt{2}}{3\pi}\left(\frac{E_t}{d^2 p}\right) \qquad (2)$$

d = Gas particle diameter (m)
p = Gas pressure (Pa)

The thermalization distance (D) can be calculated using the mean free path and the number of collisions required to slow the sputtered particles to the average gas thermal velocity.

$$D = \lambda\, \eta^1 \qquad (3)$$

$\lambda$ = Particle mean free path (m)
$\eta^1$ = Particle collisions (unitless)

The number of collisions needed for thermalization ($\eta^1$), assuming directionality of the starting atomic flux, is[26]

$$\eta^1 = \frac{\ln(v_g / v_o)}{\ln\left[\frac{1-M}{1+M} + \frac{2M}{1+M}\frac{\ln\left[(1+M)^{1/2} + M^{1/2}\right]}{4M^{3/2}(1+M)^{1/2}} + \frac{2M^4 + 5M^3 + 3M^2 - M - 1}{4M(1+M)^3}\right]} \tag{4}$$

where $v_g$ = thermal velocity (m/s) and is taken to be $v_g = \sqrt{\frac{3k_B T}{M_g}}$, (5)

$v_o$ = initial velocity (m/s) and is approximated by $v_o = \sqrt{\frac{qV}{M_g}}$, (6)

and $M = M_g$ (gas particle mass, kg) / $M_s$ (metal particle mass, kg). (7)

$\eta^1$ is approximately 1.8 for the range of deposition parameters in this work.

The Faraday dark space occurs when the electron kinetic energy drops below the gas ionization energy. The positive column, when present, occurs when the electrons regain sufficient kinetic energy to effect gas ionization. It is typically not seen in glow discharges optimized for sputtering where the target to substrate spacing is minimized to improve film deposition rates. The plasma voltage drops to the anode voltage in the anode dark space. The anode is typically the rest of the deposition system, and is grounded. The substrate may be clipped directly to a holder on the anode, or may be biased. The anode field accelerates ions towards the anode, but the effect is much less pronounced compared to the cathode. A bias voltage applied to the substrate can be used to sputter the growing film surface. Substrate biasing has been reported to remove oxygen surface contaminants in DC diode sputtered TiN thin films.[27]

## 2.3 Particle flux energy

Deposition power and pressure are significant process parameters in controlling film microstructure. Both are important in determining the energy of the impinging particle flux at the substrate surface. Increased deposition power increases the cathode sheath voltage, which increases the initial energy of the sputtered metal atoms and reflected fast neutral gas particles. The working gas pressure in the glow discharge determines the mean free path of the particles. Thermalizing collisions in the glow discharge scatter the flux and reduce the particle energy; therefore, increased gas pressure reduces the flux energy at the substrate surface.

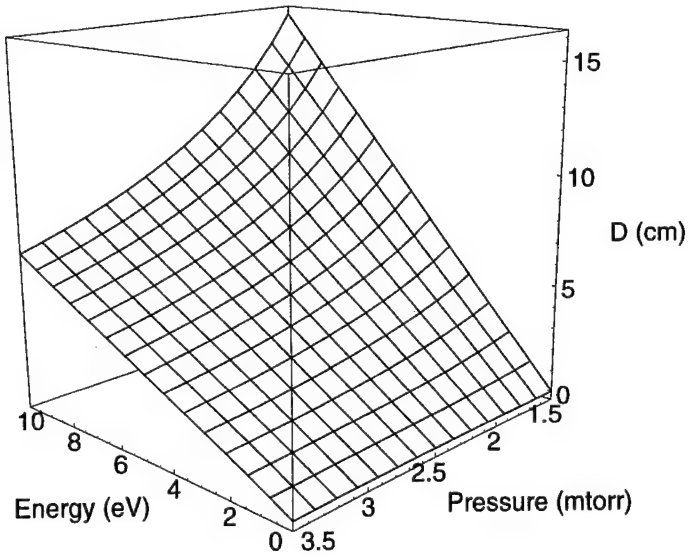


**Figure 3**: Theoretical Flux Thermalization Distance

The theoretical thermalization distance (D) can be calculated with equations (2) – (7). The plot in Figure 3 assumes the use of pure $N_2$, as diatomic $N_2$ has a larger collision cross section than Ar. The Al cross section is assumed to be 30Å; the $N_2$ cross section used in the calculation is 36.8 Å. The gas temperature used in the calculation is 300 K; the actual gas temperature is likely to be higher due to electron heating. It is important to note that the particle energy distribution in equation (1) determines the proportion of particles having a given translational kinetic energy (Figure 4). The peak of the kinetic energy distribution increases with incident ion energy, which is determined by the cathode sheath voltage.[28]

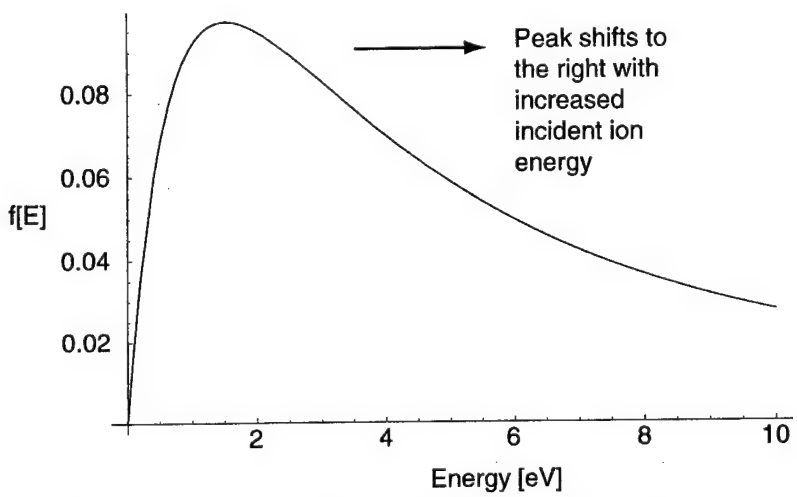


**Figure 4**: Sputtered Particle Energy Distribution Profile

2.4 Particle flux population

The reactive sputter deposition of AlN involves several particle flux populations. Of particular interest are aluminum, nitrogen, argon, and oxygen-containing contaminants. The aluminum particle flux originates at the target surface. The metal flux energy distribution is determined by the energy of the sputtering particles. The sputtering energy in turn is affected by the cathode sheath voltage. The ionized gas particles are accelerated by the cathode electric field, and an increase in the voltage results in higher sputtered particle energies.[29] Sputtered Al neutrals and ions are expected to follow a cosine law momentum distribution.[24] Reports on reactive sputtering of AlN and TiN indicate that Al and Ti neutrals comprise the dominant neutral particle flux, respectively for each material.[30,31] While metal ions are present to some extent, they do not play a significant role in film growth kinetics. The aluminum flux is subject to thermalization in the transport process; consequently, the initial particle energy profile may be altered as a function of pressure.

Nitrogen and argon are introduced into the deposition chamber via gas inlets, and the exact sources of the fluxes are dependent on the system geometry. However, the gas sources can be thought to originate at the target surface for reflected and sputtered species, and from the negative glow region for ionized species. Ar fast neutrals are formed when $Ar^+$ ions gain an electron upon impacting the target surface. The neutralized atom is reflected from the target, and is no longer subject to the cathode electric field. Nitrogen fast neutrals are thought to form in a similar manner, albeit via impact dissociation of the diatomic molecule that results in N atoms rather than molecules.[29] At low $N_2$ pressures, the flux is low while the particle energies are high. The flux increases at higher pressures, but scattering and thermalization serve to reduce the flux energy. Ionization within the negative glow is likely to produce lower energy ions, as the voltage drop across the anode dark space is lower than the voltage drop at the cathode. The ions generated in the glow are more likely to be monoenergetic than particles originating from the cathode, as the probability of collisions in the thin anode dark space is much lower.

Optical emission spectroscopy of the glow discharge in an RF magnetron reactive sputtering experiment indicate that $N_2$, and to a lesser extent $N_2^+$, are the dominant species at nitrogen concentrations in excess of 50%, while Al and Ar neutrals are present in smaller concentrations.[32] Similar findings have been reported for DC magnetron sputtering, with

excited $N_2$ and $N_2^+$ the dominant fluxes.[33] It has been suggested that the molecular $N_2$ species are primarily responsible for bombardment of the substrate surface.[30] Double-modulation mass spectroscopy of glow discharge gases in reactive sputtered TiN indicate a prevalence of monoenergetic $N_2^+$ and $Ar^+$ ions, while $Ti^+$ and $N^+$ ions followed an energy distribution that is concordant with sputter ejection. TiN and $TiN^+$ concentrations were orders of magnitude below the concentrations of the dominant particle fluxes, and were considered insignificant in film growth kinetics.[31] The same is thought to be true for sputtered AlN, where Al atoms and not AlN molecules are ejected from the target surface. The neutral Al flux reacts with $N_2^+$ ions and $N_2^*$ metastable radicals formed in the glow discharge to form AlN at the substrate surface.[30]

Contaminant fluxes are significant for nonideal deposition processes, and must be taken into consideration. The dominant contaminants in AlN deposition appear to be oxygen containing species, including molecular oxygen[9,34,35] and water vapor.[36] Outgassing from chamber walls and system components appears to be the main source of the background oxygen pressure. Oxygen containing molecules are also introduced into the deposition chamber with the process gases. Though high purity $N_2$ and Ar gases are used, some residual contamination is unavoidable. While the goal is to minimize oxygen flux to the substrate surface, it cannot be entirely eliminated. Oxygen contamination can play a significant role in degrading film crystallinity in reactive sputtered AlN films.

## 2.5 Adatom mobility and surface nucleation

The particle flux arriving at the substrate surface must adsorb to be incorporated into the film. The initial impact of the impinging particle may dissipate sufficient kinetic energy to prevent its escape from the substrate surface. The particle is loosely attracted to the substrate surface via dipole or induced dipole dispersion forces. The adsorbed atom (adatom) is able to diffuse along the surface of the substrate when physically adsorbed, or physisorbed. Chemisorption occurs when chemical bonds are formed between the adatom and the substrate. Film growth in sputtered AlN films occurs when activated nitrogen species chemisorb aluminum at the substrate surface, and vice versa.[9] The kinetics of both processes affect film growth, ensuing film microstructure, and film properties for low temperature sputter deposition.

Adatom mobility strongly affects the crystallinity of the resultant thin film. High mobility improves crystallinity by allowing adatoms to reach low energy binding sites

consistent with crystalline film growth; conversely, low mobility promotes amorphous film growth.[37] The adatom diffusion length (Λ) is indicative of its mobility, and is given by equation (8).[38]

$$\Lambda = a\sqrt{\frac{\left(\frac{k_B T}{\hbar}\right) n_o}{J_r}}\, e^{-E_s/2RT} \qquad (8)$$

$a$ = distance between sites (nm),
T = temperature (K),
$n_o$ = number of adsorption sites (sites/cm$^2$),
$J_r$ = deposition flux (molecule/cm$^2$ s),
$E_s$ = transition state energy barrier (kJ/mol)

As the transition state energy barrier increases, the diffusion length decreases exponentially. The type of interaction between the adatom and the surface determines the transition state energy barrier. Dispersion forces are relatively weak, with the enthalpy of adsorption on the order of 5-20 kJ/mol.[38,39] Chemisorption energy barriers are significantly higher (e.g. Al-N bond energy is 297±96 kJ/mol; for the Al-O bond, it is 512.1±9.2 kJ/mol);[40] chemisorbed atoms are effectively immobilized for room temperature sputtering processes. Raising the surface temperature increases the adatom mobility. Early microstructure zone models propose changes in the sputtered film microstructure as a function of $T/T_m$, where T is the substrate temperature and $T_m$ is the melting point of the material.[41] Ion-bombardment of the growing film surface has been proposed as a means by which adatom mobility is increased.[42] Fast impinging particles are thought to transfer a portion of their momentum to diffusing adatoms at the film surface, promoting adatom mobility.

Heightened surface roughness impedes adatom mobility, and has been identified as a factor in reducing film crystallinity in this study (section 4.3.1). The presence of surfaces disrupts the ordered structure of crystalline solids, resulting in numerous dangling bonds. Increasing the surface roughness results in a larger surface-area-to-volume ratio, increasing the dangling bond density and decreasing the distance between potential binding sites. Surface diffusion of adatoms is hampered by interaction with the reactive dangling bonds on the substrate or film surface.

Oxygen contamination at the film surface can also decrease the adatom mobility. On the basis of bond energy, the formation of Al-O bonds is preferable to the formation of Al-N bonds. The presence of oxygen at the film surface acts to reduce the average diffusion length of Al adatoms. A high oxygen partial pressure during film growth promotes amorphous film growth at low deposition temperatures by diminishing the adatom surface diffusion length.

| | Surface roughness ($R_a$) | 80°C | 200°C |
|---|---|---|---|
| Minolta HTO | 0.5 nm | 7 (μm) | 15 |
| Novellus LTO | 1.6 nm | 5 | 10 |
| Novellus Nitride | 3.6 nm | 21 | 25 |

**Table 2**: Al Diffusion Distance as a function of Substrate Temperature and Material[43]

Scanning auger microscopy of aluminum diffusion on oxide and nitride surfaces reveal substantial differences in the diffusion lengths (Table 2). Surface roughness and substrate temperature effects are also evident in the study, in comparing results for high temperature oxide (HTO) and low temperature oxide (LTO) surfaces. Several reports have indicated that AlN films with high oxygen content are less crystalline than low oxygen or oxygen-free films.[35, 44]

Film nucleation is kinetically constrained by adatom mobility where $\Lambda < a$, and quenched growth is favored.[45] Quenched growth results in Z1 film microstructure, with amorphous or poorly crystalline microcolumns (~10 nm diameter) separated by voids (~1 nm). The microcolumns aggregate to form conical structures (~40 nm diameter) in thicker films. The cones terminate in domes at the film surface. At high temperatures, $\Lambda >> a$ and film nucleation is dictated by thermodynamic considerations. AlN films deposited on high temperature Si substrates (T=800°C, $T/T_m$=0.43) via PEMBE and DC magnetron reactive sputtering exhibited Volmer-Weber (VW) type growth.[16, 46] VW or island type growth begins with 3D film nucleation and results in Z2 film microstructure. The Z2 microstructure contains facetted crystalline columns with minimal intercolumnar voids.[16] The intercolumnar voids are decreased due to improved surface and bulk diffusion. A transitional zone, ZT, exists between Z1 and Z2 for energy-enhanced deposition. ZT microstructure comprises microcolumns seen in Z1 films, without the conical structures and large internal voids. Z1 or ZT microstructures are expected for low temperature (less than 200°C) reactive sputtered AlN films.

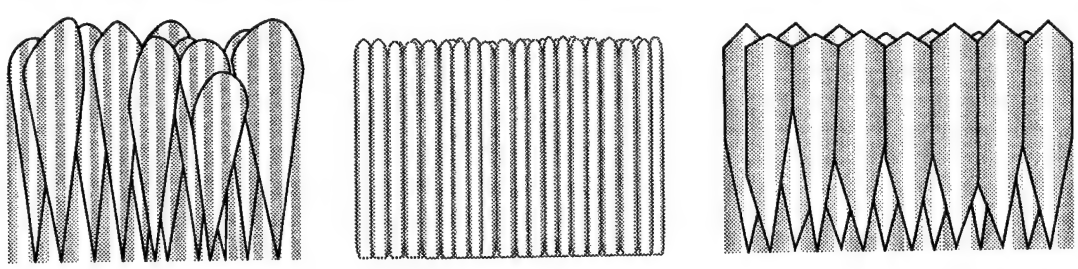

Zone 1 Zone T Zone 2

**Figure 5**: Z1-ZT-Z2 Microstructures for DMT Zone Model

## 2.6 Film growth and modification

Changes in film microstructure occur throughout deposition. The final film microstructure and properties are affected by these changes. Film modification mechanisms that operate during the growth phase may be kinetically constrained by the substrate temperature. Thermodynamic effects which are significant in high temperature epitaxial growth may not be observed for low temperature reactive sputtering. The contribution of each mechanism is difficult to gauge experimentally with the existing deposition apparatus. The film modification mechanisms operate simultaneously, and effects are likely to be convoluted. The scope of the present study is limited to the identification of film modification mechanism as they pertain to the thesis objectives.

Substrate matching is significant in epitaxial AlN growth. Mismatched lattice constants and differences in thermal expansion coefficients affect resultant film crystallinity. The substrate crystallinity or absence thereof in amorphous substrates also affects film quality. X-ray diffractometry of films grown on various substrate types using ECR PECVD at 500°C ($T/T_m$=0.31) indicates that films deposited on Si (100) and (111) substrates are more crystalline than films deposited on amorphous substrates ($SiO_2$ and $Si_3N_4$). The most crystalline film in the study is deposited on (0001) $\alpha$-$Al_2O_3$, which has the least lattice mismatch with (0001) AlN.[47] The presence of a native oxide on the Si substrates is noted, and is thought to affect c-axis orientation in the AlN films. Due to the lower temperature range used in the present study, substrate matching is not likely to play a significant role in film crystallinity, as other factors overshadow the effect of mismatched lattices. However, differences in thermal expansion coefficients between AlN and Si (100) are expected to contribute to film stress.

Flux induced film modifications are affected by the energy profile and thermalization distance of impinging particles. Ion peening of the growing film surface suppresses Z1 microstructure while imparting a compressive stress to the film. The effect is analogous to shot peening of sheet metal on the macroscopic scale. Film densification occurs when impinging particles collapse film voids. Ion bombardment also effects energy transfer to surface adatoms, which increases their mobility and surface diffusion. However, the effect is not significant where the flux is thermalized or scattered before reaching the substrate surface. The mean free path of $Ar^+$ ions was calculated to increase from ~1 to 10 cm as the glow discharge pressure drops from 1 to 0.1 Pa (7.5 mtorr to 0.75 mtorr).[48] At the other extreme, highly energetic Ar

atoms may be implanted into film. Implanted ions cause compressive stress, which offsets tensile stress from microvoids. However, ion implantation can also degrade film crystallinity.

In addition to ion peening, an energetic particle flux can also sputter the growing film surface. Experimental evidence indicates that the high surface energy planes are preferentially sputtered, leading to the development of film texture in polycrystalline thin films.[49] The anisotropic etching favors low Miller index planes, including the (0001) basal plane in wurtzitic materials. Sputtering of the film surface can be enhanced through substrate biasing. The redistribution of film material helps to reduce the film surface roughness by filling in voids.

Self shadowing is a process which operates to increase film surface roughness. Existing surface peaks receive greater incoming particle flux, leading to heightened growth. Regions between peaks receive little incoming flux because they are shadowed, and develop into voids. Self shadowing is responsible for the columnar voided microstructure seen in Z1/ZT films.[41] It has been proposed that atoms captured via self shadowing by an existing grain help to develop the in-plane texture of the grain.[49] Molecular dynamic simulations indicate that the shadowing effect is statistical in nature in that the random arrival of particles will result in peaks and valleys even if the initial surface is atomically smooth.[50] Surface diffusion and resputtering counteract self shadowing by allowing atoms to fill voids while they are being formed. The substrate temperature, flux energy, and flux thermalization distance are important in overcoming shadowing effects and reducing film voids.

Voids in the film may be also be reduced by bulk diffusion which occurs while the film is still growing. Atomic diffusion into voids and along grain boundaries act to reduce film porosity provided that the substrate temperature is adequately high. Substrate heating during film deposition may act to increase the rate of bulk diffusion and thereby improve film quality. The substrate temperature and annealing time are important for bulk diffusion.

The presence of a growing film surface containing numerous voids introduces additional complications with regards to contaminant fluxes. Given the reactivity of oxygen with aluminum, O incorporation occurs at the film surface and along intergranular voids where Al is available for bonding . At high oxygen concentrations, $Al_2O_3$ phases may form and disrupt the AlN structure.[35, 51] Lower concentrations of oxygen has been reported to form AlON polytypoids and $O_N/V_{Al}$ defects in bulk AlN studies[52]. As oxygen outgassing in the deposition chamber is affected by the sidewall and substrate temperatures, increasing the

substrate temperature has the unfortunate side effect of increasing the oxygen flux as well. Increasing the substrate temperature may increase the surface and bulk diffusion rate for the growing AlN film; at the same time, it increases the oxygen outgassing rate through incidental heating of the chamber walls. The two effects are convoluted, making an accurate assessment of the actual process rather difficult.

## 2.7 Film microstructure and properties

Processing conditions dictate the resultant film structure, which ultimately affects properties of interest. For MEMS application, the piezoelectric coupling strength of the film is a critical film property. Other film properties affect device performance and reliability (e.g. stress and uniformity) or subsequent processing steps (e.g. surface roughness). The film structures at the lattice, grain, and crystallite level are responsible for these film properties.

The piezoelectric effect originates at the unit cell level, and is contingent on the absence of inversion centers in the lattice. Based on this criterion, an amorphous film cannot be piezoelectric due to the presence of long range inversion symmetry. Film crystallinity is therefore a fundamental requirement for film piezoelectricity. Experimental evidence indicates that increased piezoelectric response and decreased surface acoustic wave (SAW) insertion loss is observed in films with greater crystallinity as measured by x-ray diffractometry.[34, 53]

Though crystallinity is necessary for piezoelectricity and an empirical relationship exists between the two, correlation does not demonstrate causality. Several mechanisms have been proposed regarding the relationship between film crystallinity, piezoelectric response, and oxygen content. The deleterious role of oxygen contamination on adatom mobility and its effect on film nucleation and growth was discussed in earlier chapters. Neglecting voids, decreasing the average grain size in films with a columnar microstructure causes the grain boundary area to be inversely proportional to the grain radius. As the grain boundary represents a break in the crystalline order within the grain, the volume of material within several unit cells of the grain boundary is unlikely to be piezoelectric. Average grain size, regardless of grain morphology, is expected to be correlated with film crystallinity and piezoelectric response if this mechanism is dominant.

An *ab initio* study found that oxygen substitution in the nitrogen sublattice is energetically favorable, and the presence of $O_N$ leads to $V_{Al}^{3-}$ compensating defects.[54] Bulk studies of sintered AlN indicates that the oxygen accommodating site undergoes a transition at

oxygen concentrations at 0.75 at. % to form octahedrally coordinated Al-O structures . At higher oxygen concentrations, inversion domain boundaries (IDB's) comprised of octahedrally coordinated Al-O structures are thought to be energetically favorable.[52] The oxygen defect model has been proposed for grain and crystallite structural changes in sputtered AlN thin films.[44] IDB formation is highly relevant where film piezoelectricity is the property of interest. Introducing an inversion center into the film material causes localized degradation of the piezoelectric response by reversing the dipole polarity across the domain boundary. This effect should hold true even in epitaxial films where grain boundaries do not play a significant role. Film oxygen content is expected to noticeably alter film piezoelectric response if this is the case.

It should be noted that the two mechanisms are not mutually exclusive. Instead, the two are likely to be linked in low temperature sputter deposition of AlN. The presence of oxygen containing contaminants simultaneously reduces grain size and increases the oxygen content of the films. Deconvolution of the effects and assessing their individual contribution to decreased crystallinity or piezoelectric response is beyond the scope of this project, and is necessarily reserved for future work.

Film stress is affected by film structure at several levels. The primary source of tensile stress in sputtered AlN films is microvoids between crystallites. Computer simulation indicates that the collapse of large voids between columnar crystallites causes short range attractive forces to act across resultant microvoids.[50] The effect is suppressed by film densification during growth by ion peening, which eliminate large voids between crystallites before they develop fully. Self shadowing increases voided film volume where ion peening and surface diffusion are negligible. As self shadowing becomes more prominent throughout film deposition, an increase in film tensile stress or decrease in compressive stress as a function of film thickness can be expected. The effect was observed by *in situ* monitoring of intrinsic film stress, where films grown at 5.1 and 9.2 mtorr were initially compressive and later became tensile.[46] Interestingly, the film grown at 2.3 mtorr remained compressive with increased thickness. Additional empirical support for the microstructure-stress model is found in numerous studies which report increased compressive stress with decreasing deposition pressure for ZnO and AlN deposition.[55, 56] Microstructural studies of sputtered ZrN and AlN also support the ion peening model as described above, with highly compressive films that

become significantly less compressive with increased working gas pressure.[57,58] The Z1 microstructure is held to be too porous to sustain stress, while ZT is capable of sustaining tensile stresses.

Several mechanisms have been suggested for the compressive stress observed in sputtered AlN films. Molecular dynamics simulation and experimental results of sputtered W films suggests that Ar incorporation contributes to the compressive stress.[25] However, the magnitude of compressive stress in sputtered Mo films correlates with the presence of Ar and not the magnitude of entrapped Ar.[59] The presence of oxygen in sputtered metal films has been reported to increase compressive stress, but the role of oxygen in promoting film stress in AlN films remains unclear.[60] Modifications to the film microstructure by oxygen probably outweigh any stress contributions at the lattice or grain level.

## 3. EXPERIMENTAL

### 3.1 Design

Response surface methodology (RSM) in experiment design offers certain advantages over classical single variable experimentation.[61] The classical approach presupposes that interactions between process parameters do not significantly affect the system output. This is often not the case for physical systems. For this reason, single variable experiments can produce misleading results when used for process optimization. Designed experiments improve on the classical approach by taking into account interaction between variables. The response surface is fitted to the data points throughout the parameter space, allowing one to accurately identify maxima and minima in film properties within the range. The curvature of the response surface suggests changes in the process parameters for property optimization.

A six-factor rotatable central composite designed experiment forms the basis of this work. The design is rotatable with $\alpha$ equal to 2.828, where $\alpha$ is the distance between the center point and axial points on the parameter axes. The six process parameters and their ranges used in the experiments are: plasma power (0.5-2.5 kW), gas pressure (1.5-3.5 mtorr), gas flow rate (20-60 sccm), gas composition (50-100% $N_2$, remainder Ar), initial substrate temperature (25-175°C), and supplemental heater power (0-100%). Most parameter ranges are selected based on system constraints, except gas pressure. The pressure range was selected based on prior screening experiments, which indicated that deposition conditions producing high film crystallinity tend to occur at low deposition pressures (full gas pressure range being 1.5-10 mtorr). Experiments were divided into five blocks to account for systematic changes that may have occurred when the deposition apparatus and material are modified.

The cathode sheath voltage dictates the energy distribution of the neutral Al and N by changing the initial energy with which sputtering gas particles sputter the target surface. The magnitude of the flux can be approximated by the measured discharge current. Charge transfer occurs when sputtering gas ions strike the target surface and become neutralized, and also when secondary electrons are emitted. The current flow is therefore proportional to the sputtering ion density. The plasma power setting affects the discharge voltage and current density. The target power supply operates in constant power mode, which is potentially unstable due to surface nitridation. Target nitridation has been reported to decrease the discharge voltage.[9] Under constant power operation, decreasing the discharge voltage causes the current to increase. The

increase in current concurrently augments the nitrogen ion flux to the target surface, which results in additional nitride coverage. The presence of Ar in the working gas is an additional variable to be taken into consideration. Ar sputtering removes the surface nitride and exposes the underlying metallic surface. It is difficult to predict the surface evolution over the course of deposition based on these considerations.

Observation of the cathode voltage profile indicates that the operating voltage is stable above 20 sccm $N_2$ flow (50% $N_2$-50% Ar) at 1.7 mtorr and 1.0 kW. The instability in cathode voltage appears to occur at 12 sccm $N_2$ flow (30% $N_2$), which is below the range of nitrogen partial pressures used in the designed experiment. Target presputtering allows the voltage to stabilize prior to film deposition. Moreover, experimental evidence in the literature suggests that no hysteresis or voltage transitions are observed when the gas partial pressures are kept constant,[9] which is the case in this work. The sputtered neutral particle flux energy and magnitude should remain constant over the duration of film deposition.

The gas pressure determines the particle mean free path within the glow discharge. The gas pressure is controlled in the deposition apparatus by gas flow and dynamic pumping. Ar and $N_2$ are introduced via precision mass flowmeters, and removed by a cryogenic pump. A baffle valve between the deposition chamber and the pump serves to control the pumping rate. The arrangement allows the system pressure to be decoupled from the flow rate, to an extent. Very high flow rates (in excess of 60 sccm) impose a minimum deposition pressure around 1.5 mtorr. The film microstructure and properties are expected to respond to changes in the deposition pressure due to its role in thermalizing the impinging sputtered particles.

Changing the settings on the Ar and $N_2$ flowmeters controls the gas flow rate and overall discharge plasma composition. The composition affects the target nitride coverage, as well as the sputtering efficiency of the working gas. High flow rates may reduce the oxygen partial pressure at the target surface by sweeping outgassed contaminants into the cryogenic pump. As oxygen contamination is expected to degrade film properties of interest, even a marginal reduction in the oxygen concentration is of value.

Substrate heating is implemented in this work through procedural and hardware modifications. The initial substrate temperature is controlled by preheating the substrate in the load lock with quartz heat lamps. The temperature is ramped up over a period of 20-30 minutes and then held at the target temperature. Feedback is obtained by thermocouple contact to the

stainless steel substrate holder. The substrate is assumed to be in thermal equilibrium with the holder; initial temperature measurements are expected to be accurate within ±0.2°C based on thermocouple instrumentation limitations.

The substrate begins cooling when it is introduced into the deposition chamber. The initial temperature and the amount of time it takes to initiate film deposition affect the actual starting substrate temperature. Consistency in the lag time is critical to ascertain temperature effects, and is an experimental objective. Measurement of the substrate temperature during deposition poses a number of difficulties. The glow discharge is electronically noisy, rendering thermocouple probes near the substrate useless. Noncontact methods including infrared pyrometry are difficult to implement because optical windows near the sputtering source tend to be coated over time. Consequently, a single quartz lamp heater covered by a shutter is used to provide additional heating during deposition to offset heat loss. The final process variable is the power supplied to the heat lamp during deposition. Efficient radiant transfer of thermal energy from the lamp to the substrate holder is assumed. As the plasma contributes thermal energy to the film as well, it is difficult to estimate the actual deposition temperature. Previous reports indicates that plasma heating contributes minimally to the initial substrate temperature, on the order of 70°C.[14] The substrate temperature does not exceed 250°C for the present work by backward extrapolation of chamber thermocouple data.

The film analysis will be divided into two tiers based on their significance to MEMS device fabrication and ability to provide underlying information on the deposition process, film microstructure, and film properties. Response surface analysis will be applied only to the top tier of material properties due to time and resource considerations. Primary analysis will survey film crystallinity, stress, and thickness uniformity for all samples. Crystallinity provides an assessment of the film piezoelectric response. Film stress minimization and uniformity in deposition are useful in MEMS device fabrication, and will be considered. Secondary analysis will focus on subsets of the film samples to elucidate additional information, such as film composition and microstructure, where the additional information may link film property to specific microstructural features.

3.2 Apparatus

A modified Perkin-Elmer 4410 DC magnetron sputtering system was used to reactive sputter piezoelectric AlN thin films on Si (100) substrates. An ultra-high purity Al delta bolt-on target (99.999%, Tosoh SMD) was installed in the system for this work. Filtered Ar (ULSI grade, BOC) and $N_2$ (6.0 grade, Airco) were used to minimize contaminants in the working gas. To provide temperature control, the system is fitted with quartz heat lamps in the load lock and deposition chamber. In addition, the chamber wall is fitted with a water jacket that can be used to assist in the chamber bakeout. The mean chamber base pressure was $5\times10^{-8}$ torr over the course of the experiment. Reduction of the base pressure was attained partly by the removal of the substrate carrier motion feedthrough, fixing the target-substrate spacing at 10 cm.

MEMS device wafer processing begins at Draper Laboratory. The sputtering system is used to deposit a 0.5-μm AlN film on Si (100) membranes, then returned to Draper Laboratory for further processing. Untreated Si (100) test wafers (Wacker Siltronic, *p*-type, 510-540 μm thick, 7.0-10.2 Ω) were used for the designed experiment. The device wafer membranes typically undergo some etching prior to AlN deposition; the test wafers are rinsed in deionized water and spin-dried in $N_2$. The native oxide on the test wafers is left in place, as removal via etching increases surface roughness. The difference in surface roughness between the device wafers and the test wafers can produce noticeable differences in the predicted film properties (Section 4.3.2).

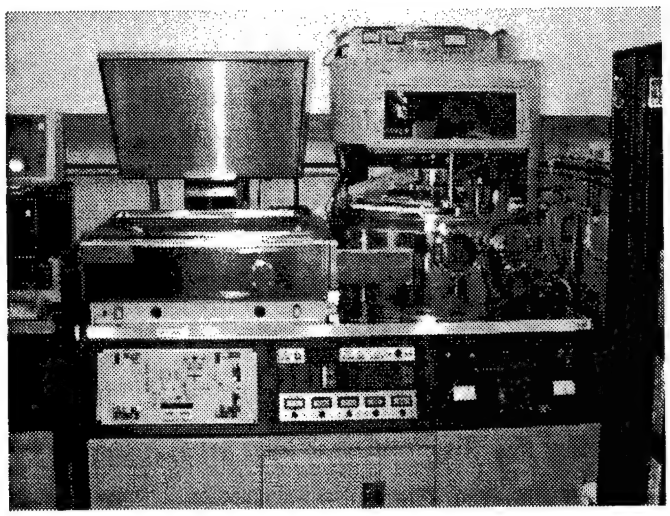

**Figure 6**: Modified Perkin-Elmer 4410 DC Magnetron Sputtering System

3.3 Deposition protocol

Predeposition chamber conditioning is performed prior to AlN film deposition. The target is sputtered for 30 minutes (1.0 kW, 4 mtorr, 40 sccm, 100% Ar). The step serves to clean the target surface of nitrides and to coat the inside of the deposition chamber with 2-3 μm of Al. The sputtered Al getters the oxygen present in the chamber and seals off outgassing sources.[9,62] The inside of the deposition chamber is coated with a fresh layer of Al thin film and effectively acts as a getter pump for oxygen during film deposition. Residual gas analysis is used following chamber conditioning to assess the oxygen partial pressure (typically below detection limit, less than $10^{-10}$ torr). The target is then sputtered for 10 minutes in $N_2$ (1.0 kW, 1.5 mtorr, 40 sccm, 100% $N_2$). The deposition of a thin AlN layer produces a thin diffusion barrier against $H_2O$ diffusing in from the chamber wall, which is water cooled. The steps combine to produce a standard nitrided surface for all depositions, reducing the likelihood of voltage transitions due to coverage effects discussed in the previous chapter. Substrate preheating in the load lock occurs concurrently with the chamber conditioning steps. The temperature is ramped over 20-30 minutes until the desired temperature is reached. The heating is then reduced to hold the substrate at the target temperature. Substrate temperature is typically within 3°C of the target temperature at the time it is moved into the deposition chamber.

The substrate is moved into the chamber against positive gas pressure (0.15 mtorr) to prevent contamination from the load lock. Additional substrate heating begins when the substrate enters the chamber. The chamber is pumped down to $10^{-8}$ torr before being backfilled with working gas at deposition flow rate, composition, and pressure. The target is sputtered for 5 minutes at deposition power with the target shutter closed. The deposition timer is started and the plasma I-V values are recorded when the target shutter is fully open. The deposition time is calculated from deposition rates determined in previous experiments. The shutter is closed when the film reaches ~0.5-μm. The target power is shut off, and the target surface ceases to react with $N_2$.[9] At this point, a pressure increase occurs. The $\Delta P$ corresponds to the partial pressure of $N_2$ consumed during deposition, and is recorded. The $N_2$ flow is then shut off. Assuming that the cryogenic pumping of $N_2$ and Ar function independently at within the deposition pressure range, the pressure reading corresponds to the partial pressure of Ar. The chamber supplemental heating source is turned off, and the substrate temperature measured (in

later depositions, as the chamber thermocouple was not installed for the first half of the experiments). The substrate is then transferred to the load lock, again with positive pressure from the chamber. The load lock is brought to atmosphere and a new wafer loaded for deposition. The load lock is baked with heat lamps approximately 30 minutes after pumpdown. This is to reduce the load lock base pressure and reduce the likelihood of chamber contamination. The deposited AlN films typically have an iridescent appearance, a reflective blue at the center that fades into red at the edges. The color of the film is a function of the optical path, and is highly sensitive to changes in the index of refraction ($n$) and film thickness ($d$). Visual inspection of the film can provide useful information on film uniformity for films with thickness less than 0.8-μm.[63]

3.4 Film analysis

Spectroscopic ellipsometry is used to measure the resultant film thickness and index of refraction. The film thickness provides information on the film deposition rate. The mean film thickness is used in conjunction with wafer profilometry curvature values to calculate film stress. It is also used with x-ray diffractometry to determine the normalized diffraction intensity.

Profilometry is performed at Draper Laboratory to determine wafer curvature. The curvature values are compared to pre-deposition values. Laser wafer deflection measurements are also performed, but pre-deposition values are unavailable due to cleanroom operation requirements. Laboratory regulations stipulation Piranha (sulfuric acid-hydrogen peroxide) etching for wafers returned to the cleanroom after exposure to unfiltered air. This would result in roughened substrate surfaces and may change the measured wafer stress, which is undesirable. Direct transfer from cleanroom to cleanroom avoids the problem with profilometry, but as the Flexus system was not in a cleanroom environment, this was not possible for laser deflection measurements. The wafer is cut to provide x-ray diffraction samples after stress measurements are completed.

X-ray diffractometry is performed using powder diffraction (Bragg-Bretano) geometry. The AlN film exhibits $c$-axis orientation perpendicular to the substrate surface, and typically only the AlN (0002) peak is seen in a $\theta$-$2\theta$ scan. The maximum peak intensity is recorded, then

the detector is fixed at the 2θ producing the maximum intensity. The sample is then rocked about θ to determine the rocking curve full width at half maximum.

Tapping mode atomic force microscopy is performed on a subset of the films deposited in this study to obtain information on the film surface morphology. Cross sectional morphology is determined by fracture surface scanning electron microscopy. X-ray photoelectron spectroscopy with depth profiling is performed on a very small subset of samples to survey film composition and stoichiometry. Microstructure and composition analysis were performed largely to confirm trends observed in x-ray, stress, and uniformity data.

Qualitative device performance data is provided by Draper Laboratory on processed device wafers. The presence or absence of device response is taken to be the final test of AlN film quality for MEMS application. While quantitative data is available, interpretation of device output data is complicated by additional processing steps following AlN deposition and uncertainties in modeling device output. Therefore, only the qualitative aspects are considered.

3.5 Potential sources of error

The chamber base pressure is determined by the outgassing rate, which is an uncontrolled variable. The outgassing rate depends on a number of factors, ranging from wall temperature to previous exposure to atmosphere. The base pressure stabilizes after several film depositions, and ranged between $1.4\times10^{-8}$ and $7.7\times10^{-8}$ torr for the entire experiment. The oxygen partial pressure was assumed to be constant, at $\sim10^{-10}$ torr; however, this assumption may not be true when the chamber was recently exposed to atmosphere. The chamber was vented several times during the experiment for hardware repairs and modifications, which may contribute to deviations in the measured film properties.

The target voltage drifts during the course of deposition by several volts. The increase in voltage ranges from 4-6 V, which is 1-2% of the typical discharge voltage of 300V. The pressure feedback control is accurate to within 0.01 mtorr, though corrective steps may deviate from the target pressure by up to ±0.05 mtorr. The duration of the corrective steps is short, typically only 20-30 seconds. The flowmeters are assumed to be accurate to within 0.1 sccm. These process parameters are regarded as controlled, but some error is inevitably introduced by the variations.

The initial substrate temperature is controlled by preheating the substrate holder with quartz heat lamps. The temperature is monitored by a thermocouple in contact with the holder.

The temperature is ramped up over 20-30 minutes. At times, the temperature is higher or lower than the target temperature. The actual substrate temperature is noted when this is the case and the experiment continued. When deviations occur, they are typically within ±3°C of the target temperature. However, four or five runs deviated by up to +15°C. The temperature deviations are expected to add to the standard error of the data response surface model.

The substrate temperature ceases to be actively monitored once the load lock thermocouple breaks contact with the substrate holder. The substrate temperature during deposition is affected by several heat transfer mechanisms. Plasma heating depends on the target power and total deposition time. Gas flow over the substrate likely cools the surface. Radiative cooling via blackbody radiation depends on the substrate temperature. The only variable that can be used to alter the substrate temperature is the power input to the chamber heat lamp. However, without feedback, the best that can be done is to use different power settings. Timing of the processing steps becomes quite important in keeping the temperature consistent from run to run. Errors are introduced when the timing is disrupted. The inability to accurately account for the substrate temperature throughout film deposition increases the systematic error in the data set.

The target and magnet assembly were damaged near the completion of the axial block of the experiment, which measures the primary effect of the process variables. The target cooling pump failed, resulting in target melting and demagnetization of the ferrite magnets in the magnetron assembly. Films deposited with the damaged target and magnet assembly were inferior in crystallinity, necessitating replacement of both the target and magnets. Post-replacement films were comparable in crystallinity to the films deposited prior to the incident. Differences should be accounted for by separating pre-replacement and post-replacement data points into different data blocks; the axial block was replicated to ensure accuracy of results.

The original central composite design of the experiment called for 90 film depositions; the actual number performed in this work is 70, including axial block replicates. Four of the five blocks sufficed to attain a second order model, where interaction terms between the process parameters can be assessed. Third order effects are assumed to be insignificant, and the last factorial block was not completed. Statistically significant second order models were obtained with existing data, and the last block will not be considered in this work. However, some loss of accuracy is to be expected from the omission.

## 4. Results and Discussion

### 4.1 Property response surface

Response surface methodology is frequently used in process optimization. The technique is inherently empirical, though understanding the underlying mechanisms may assist in the interpretation of the resulting model. The technique maps changes in measured properties as a function of process parameters. Interactions between parameters are taken into consideration, in contrast to single variable experiments. Deposition conditions may be optimized by pursuing the path of maximal slope increase along the response surface.

#### 4.1.1 *Crystallinity*

Previous characterization of AlN piezoelectric response indicates correlation with the x-ray diffractometry (XRD) peak intensity[34] and rocking curve full-width at half-maximum (FWHM).[53] The film crystallinity measured in terms of the rocking curve FWHM is taken to be representative of its piezoelectric response. The approach is qualitatively substantiated by the piezoelectric response of films used in MEMS chemical sensor fabrication. Wafers with AlN film rocking curve values below 4° typically yield functional devices, while films with rocking curves greater than 6° inevitably result in defective devices. The observation is in accordance with the $K^2$ electromechanical coupling coefficient response as a function of rocking curve FWHM. The $K^2$ value remains constant until the rocking curve FWHM reaches 3.5°, and proceeds to drop off sharply above 4° (see figure 5).

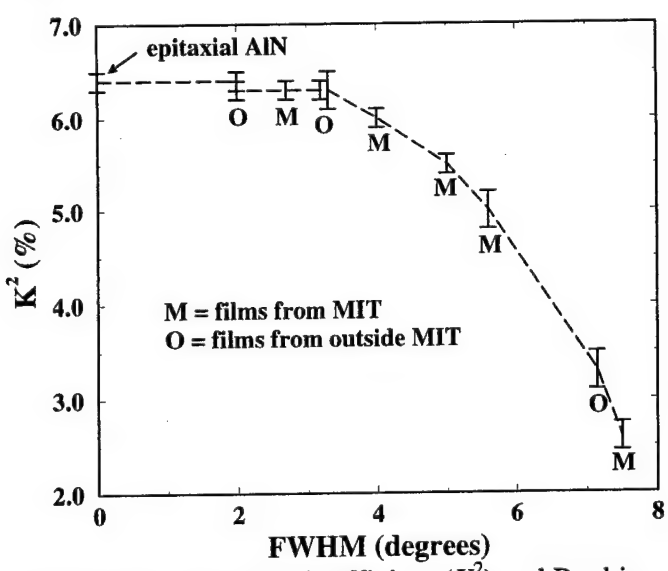


**Figure 7**: Electromechanical Coupling Coefficient ($K^2$) and Rocking Curve FWHM[53]

XRD θ-2θ scans (2θ = 33-38°) were performed on AlN film samples (1.5-cm × 1.5-cm) using the Rigaku RU300 (250 mm) diffractometer in the CMSE X-ray Diffraction Shared Experimental Facility. Peak intensity data (counts/sec) was normalized against the average film thickness (0.4-0.6 μm). The integrated peak intensity is proportional to the volume of crystalline film material having *c*-axis orientation normal to the substrate surface. The peak 2θ value (36.x°) from the θ-2θ scan is used to position the x-ray detector for the rocking curve measurement. The detector is fixed at the peak 2θ value, while the sample is rocked about the θ axis (θ = 10-25°). The rocking curve FWHM value is measured via the JADE peak analysis software. The rocking curve FWHM decreases with improved film crystalline ordering. Theoretically, the rocking curve should approach the Dirac δ-function as the film becomes more crystalline. Concurrently, the FWHM approaches 0°. The actual minimum FWHM is limited by instrument peak broadening effects. The maximum peak intensity value shows a high degree of correlation to the rocking curve FWHM value (Figure 8).

Peak intensity (arbitrary units) and rocking curve FWHM response surfaces were constructed using the Design-Expert software package (ver. 5.0.7, Stat-Ease, Inc.). Stepwise regression is used to select statistically significant process parameters. These parameters are then weighted to fit the response surface to the XRD data. The variables selected for the intensity response surface and rocking curve response surface are the same due to the correlation between the two noted in Figure 8. The peak intensity response surface is

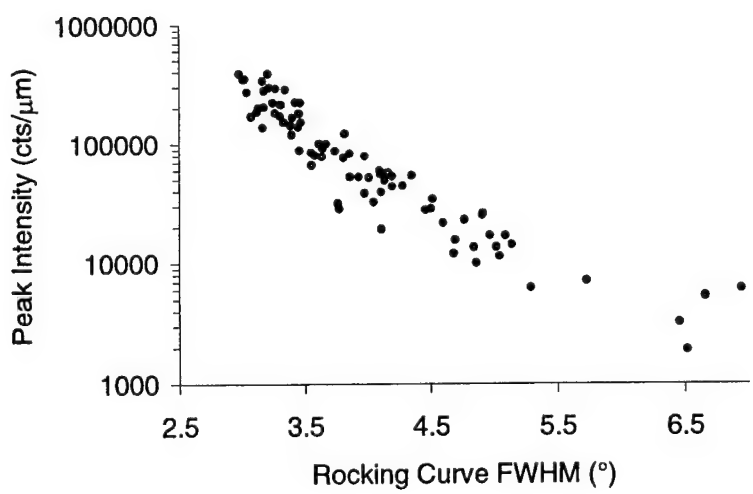


**Figure 8**: Normalized Peak Intensity and Rocking Curve FWHM

**Peak intensity** (cts/μm) = 251100 + 76326 (**Power**, kW) - 589400 (**Pressure**, mtorr)
+ 7536 (**Flow rate**, sccm) + 3289 (**Composition**, % $N_2$)
+ 1814 (**Substrate temperature**, °C) + 6086 (**Chamber heating**, % power)
+ 81786 (**Pressure**)$^2$ - 6.29 (**Substrate Temperature**)$^2$
- 140.20 (**Flow rate**) (**Chamber heating**) (9)

The corresponding response surface for the rocking curve FWHM response surface is

**Rocking curve FWHM** (°) = 9.53 - 0.26 (**Power**) + 1.37 (**Pressure**) - 0.084 (**Flow rate**)
- 0.022 (**Composition**) - 0.059 (**Substrate temperature**)
- 0.053 (**Chamber heating**) - 0.050 (**Pressure**)$^2$ + 0.0002629 (**Substrate temperature**)$^2$ + 0.001287 (**Flow rate**)(**Chamber Heating**) (10)

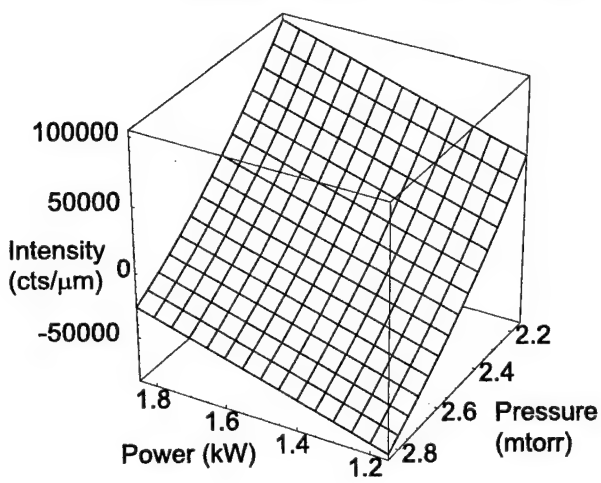


(a)

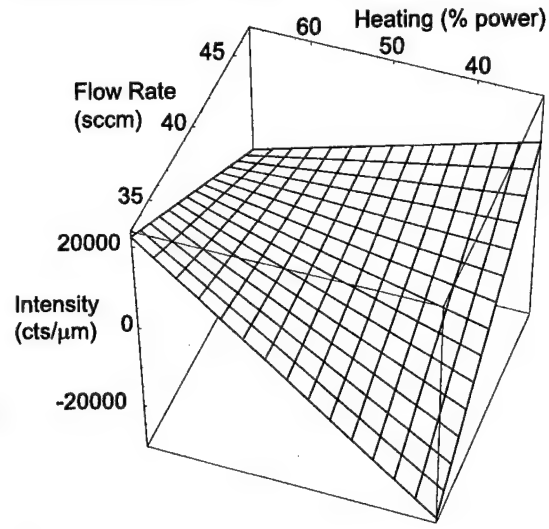


(b)

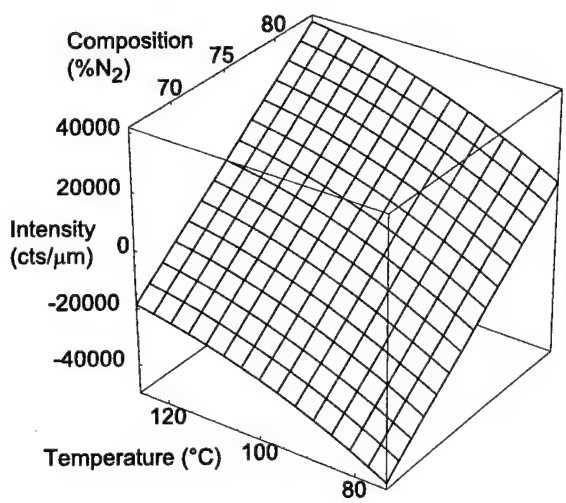


(c)

**Figure 9**: Peak Intensity Response Surface

Response Center Point (1.5 kW, 2.5 mtorr, 40 sccm, 75% $N_2$, 100°C, 50% power)=**93745 cts/μm**

(a) Deviation from center point – Power (kW), Pressure (mtorr)
(b) Deviation from center point – Flow Rate (sccm), Chamber heating (% power)
(c) Deviation from center point – Composition (%$N_2$), Temperature (°C)

(Normalized AlN (0002) peak intensity obtained by summing response center point value with process parameter deviations.)

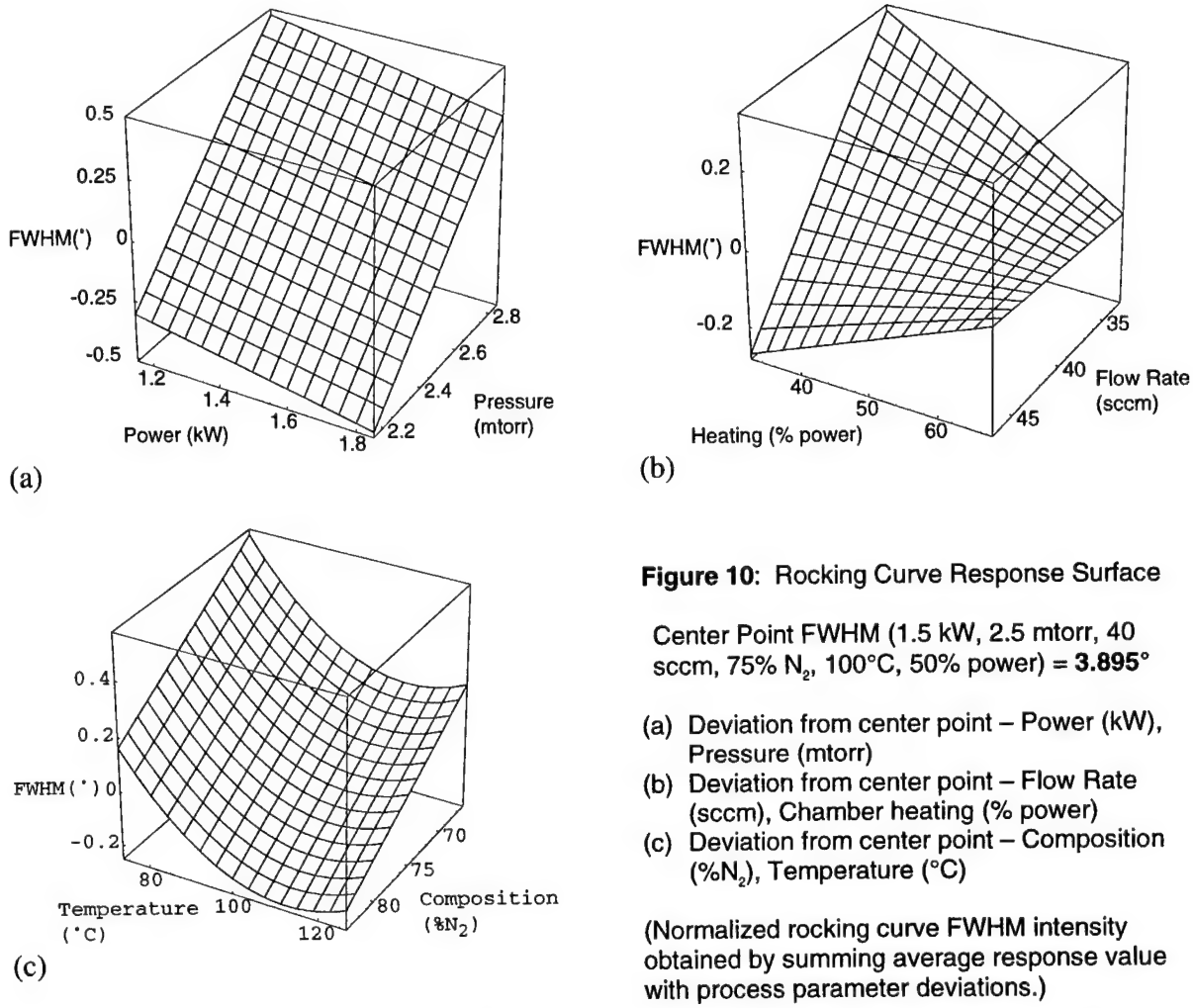


**Figure 10**: Rocking Curve Response Surface

Center Point FWHM (1.5 kW, 2.5 mtorr, 40 sccm, 75% $N_2$, 100°C, 50% power) = **3.895°**

(a) Deviation from center point – Power (kW), Pressure (mtorr)
(b) Deviation from center point – Flow Rate (sccm), Chamber heating (% power)
(c) Deviation from center point – Composition (%$N_2$), Temperature (°C)

(Normalized rocking curve FWHM intensity obtained by summing average response value with process parameter deviations.)

The deposition power and working gas pressure are the most important factors in determining the film crystallinity. Film crystallinity is improved by increased substrate temperature at low flow rates and chamber heating. This is presumably due to improved adatom mobility. The effect of changes in the flow rate is convoluted with chamber heating, which suggests the two parameters affect the chamber oxygen partial pressure. Increased flow rate reduces the oxygen residence time, while high chamber heating increases the oxygen outgassing rate. The rocking curve FWHM response surface is similar to the intensity response surface seen in Figure 9. The sign of the responses is reversed due to the inverse correlation between the peak intensity and rocking curve FWHM.

The experimental data supports the flux enhanced adatom surface diffusion model. Changes in the film crystallinity depend mainly on the deposition power and pressure, which affect the particle thermalization distance. Increasing the particle thermalization distance

increases the energy of the impinging particle flux. The resultant particle energy can also be affected by changing its starting energy. Under constant power deposition, increasing the $N_2$ gas fraction increases the degree target nitridation and the cathode voltage. Assuming that the initial particle energy increases proportional with cathode voltage and the flux is proportional to the discharge current, increasing the voltage results in a smaller, more energetic particle flux. The increase in the impinging flux particle energy augments the adatom diffusion process, producing a more crystalline film.

Substrate heating also increases the adatom mobility on the substrate surface. The initial substrate temperature significantly affects the resulting film crystallinity. High chamber heating power input helps to maintain and increase the initial substrate temperature. However, chamber heating may also cause increased oxygen outgassing. The parameter is convoluted with the gas flow rate, which affects the contaminant gas residual time. Therefore, increasing the chamber heating may increase the oxygen partial pressure, offsetting gains made by increasing the flow rate.

4.1.2 *Stress*

Film stress was measured via profilometry (Veeco Dektak$^3$ST) and laser deflection measurements (Tencor Flexus FLX 2320). Both techniques measure deflections in the Si (100) wafer due to the AlN film stress. The starting wafer curvature is measured with the profilometer only, as the Flexus laser deflection measurement apparatus is outside a clean room facility. The baseline curvature is converted from the profilometer reading to a Flexus equivalent value using an empirically derived equation relating the final wafer curvature measured on both systems.

The profilometer utilizes a stylus that scans a 5-cm track along the surface of the wafer. The wafers are measured at least twice with the profilometer, perpendicular to the primary and secondary wafer flats. Wafer flats are reference cuts in the wafer, in this case at the six and nine o'clock positions, respectively. The starting and finishing points are leveled by the profilometry software and the radius of curvature calculated by polynomial fitting of the wafer height data. Ideally, the measured radius of curvature should be equal and independent of the measurement angle as long as the track intersects the center of the wafer. This is rarely the case for pre-deposition curvature measurements. Nonuniform residual stresses often deflected

the as-received wafers into cylindrical or hyperbolic paraboloidal shapes. The post-deposition radius of curvature is typically much more uniform.

The Flexus system measures the deflection of a laser beam reflected from the wafer surface along a 10-cm track. It is used only for post-deposition curvature measurements due to clean room considerations. Each wafer is measured once with the laser deflection method. The Flexus system typically measures a larger radius of curvature compared to the profilometer, resulting in smaller stress readings. The post-deposition radii of curvature measured by the two methods are linearly correlated. As it is not possible to simply neglect the residual stress in the wafer, the empirical relationship is used to convert the pre-deposition radius of curvature obtained with the profilometer into equivalent laser deflection radius values.

The film stress is calculated using the Stoney formula.[64] The profilometer stress values and the laser deflection stress values were assessed separately. The profilometer stress response surface is given in equation (12) and the laser deflection stress model is given in equation (13).

$$\sigma = \frac{1}{6}\left(\frac{1}{R_{post}} - \frac{1}{R_{pre}}\right)\frac{E}{(1-\nu)}\frac{t_s^2}{t_f} \qquad (11)$$

$R_{post}$ = Post-deposition radius of curvature (m)
$R_{pre}$ = Pre-deposition radius of curvature (m)
E = Si modulus of elasticity (130 GPa)
$\nu$ = Si (100) Poisson's ratio (0.28)
$t_s$ = Substrate thickness (500 μm)
$t_f$ = Film thickness (~0.5 μm)

**Stress** (MPa) = 892.82 - 704.56 (**Power**) + 366.44 (**Pressure**) - 3.01 (**Composition**) + 0.30 (**Substrate Temperature**) - 102.38 (**Power**)$^2$ - 205.72 (**Pressure**)$^2$ + 419.79 (**Power**)(**Pressure**) (12)

**Stress** (MPa) = -1018.40 - 183.48 (**Power**) + 1111.90 (**Pressure**) (13)
+ 1.17 (**Substrate Temperature**) + 7.92 (**Chamber Heating**) - 189.49 (**Power**)$^2$ - 332.56 (**Pressure**)$^2$ + 320.63 (**Power**)(**Pressure**) - 0.072 (**Chamber Heating**)$^2$

Deposition power, pressure, and substrate temperature were found to be significant process parameters in both models via stepwise regression. Gas composition and chamber heating are significant for the profilometer and laser deflection stress models, respectively. The mismatch between the AlN and Si coefficient of thermal expansion is likely to be responsible for the substrate temperature and the chamber heating parameter dependence.

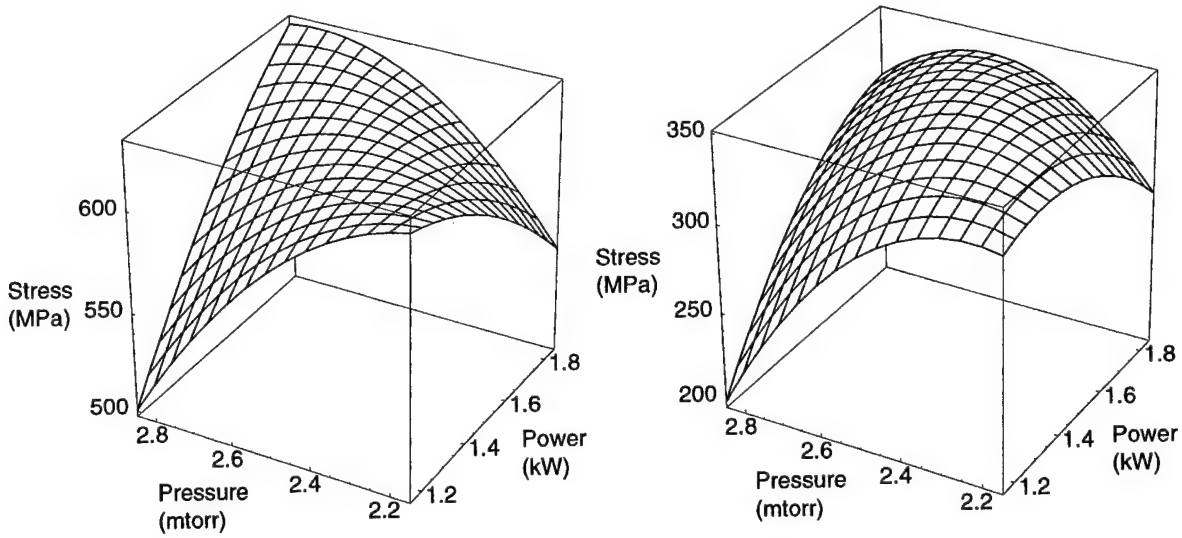


**Figure 11**: (a) Profilometry Stress Response Surface (b) Laser Deflection Stress Response Surface

Microstructural changes in the film due to ion bombardment provide an adequate explanation of the stress response surface as a function of deposition power and pressure. Molecular dynamic simulations of porous Z1/ZT films suggest several microstructural causes for film stress.[50] Highly porous Z1 films are incapable of sustaining large stresses and are formed when the impinging particle flux is low in energy. Increasing the ion bombardment energy causes the large intercolumnar voids to collapse into microvoids and an increase in the tensile component of film stress. At higher ion bombardment energies, film microvoid content decreases while particle implantation and peening increases the compressive component of film stress. As the film microstructure moves from Z1 to ZT, film tensile stress initially increases, goes through a maximum, and eventually becomes compressive as the compressive stress component become predominant. Low tensile stress is observed in the stress response surface (Figure 11) at high deposition pressures and low deposition power. The stress increases as the pressure is decreased and deposition power is increased, resulting in a maximum before decreasing at still lower deposition pressures and higher deposition powers. This is consistent with the microstructural transition model for film stress.

4.1.3 *Uniformity*

Film thickness is measured via spectroscopic ellipsometry (KLA-Tencor Prometrix-1280SE). The mean film thickness of a 49-point wafer map (Figure 12) is taken to be the film thickness in calculating the normalized XRD peak intensity and deposition rate. While the deposition rate is primarily a function of deposition power, the film thickness uniformity is not appreciably affected by any changes in the process parameters. The film thickness decreases from the center to edge; a 10% decrease for a 0.5-μm film is typical (Figure 13). The thickness variation is a function of the deposition system geometry. The decrease appears to be parabolic rather than linear.

Device wafer mapping was attempted without success. The variation in device designs on the same wafer and process steps after AlN deposition add numerous complications to assessing the piezoelectric uniformity of the AlN film. Performance of devices from the same wafer range from 10 dB to –30 dB. The device performance distribution is given in Figure 14, where large device outputs (~7.5 dB) are observed at the left of the wafer alongside minimal device output (-30 dB) observed at the right side of the wafer. However, a naive interpretation of the film piezoelectric properties is not possible due to differences in device design and additional processing. Extraction of the piezoelectric constant is theoretically possible from the electrical model of the resonator. This cannot be performed in this work due to the proprietary nature of the MEMS resonator model. Nonetheless, the distribution of device output

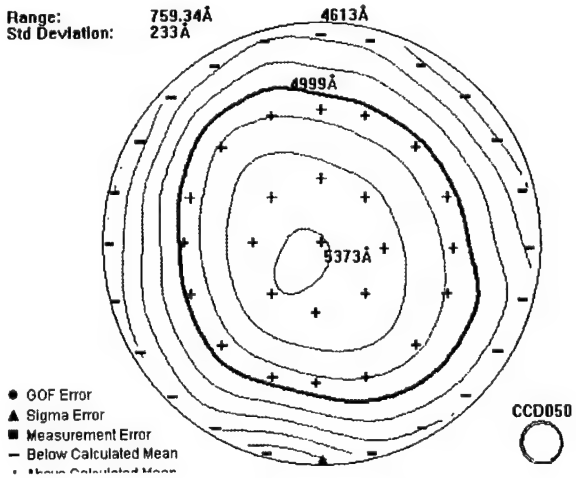


**Figure 12**: Film Thickness Wafer Map (Wafer 050 – Prometrix UV1280SE)

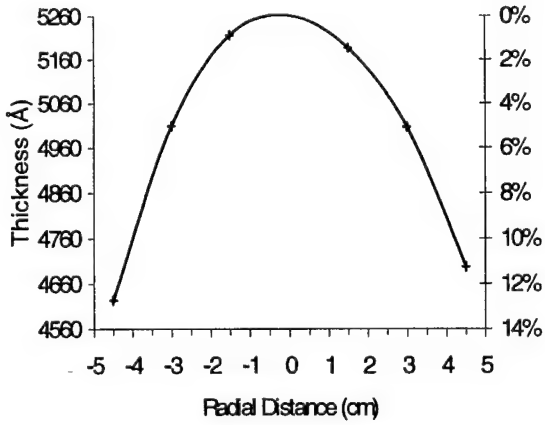


**Figure 13**: Average Film Thickness as Function of Radial Distance

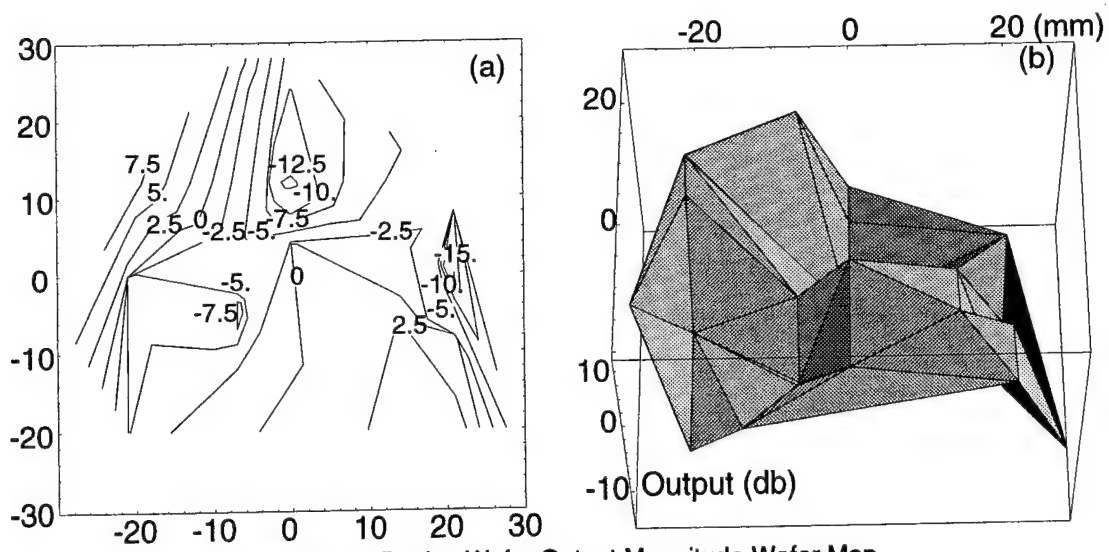


**Figure 14**: Device Wafer Output Magnitude Wafer Map
(Wafer 2507C – courtesy of Draper Laboratory)

amplitudes do not match the distribution of the other film properties examined in this study. It is possible that sources of device output variation are introduced after AlN deposition. Additonal work to identify the source of device output variations will be necessary, as the distribution of output magnitudes do not match any of the film properties mapped in this study.

## 4.2 Microstructure

Changes in the deposition parameters affect the film microstructure and properties. The stress response surface model outlined in equations (12) and (13) suggests a transition from Z1 to ZT microstructure as a function of the energy of the impinging particle flux. High energy fluxes promote adatom mobility and a dense ZT microstructure, where tensile stress due to intracrystallite microvoids is offset by argon implantation and peening. Thermalized fluxes contribute little to adatom diffusion, resulting in a highly voided Z1 microstructure. Film stress is low because due to the reduced electrostatic attraction between crystallites across the large voids, though individual crystallites may remain in tension. Sputtered films with the Z1 microstructure are less crystalline and tend to be less ordered than energy enhanced ZT films.

### 4.2.1 *Surface morphology*

Tapping mode atomic force microscopy (NanoScope IIIa, Digital Instruments) was used to characterize the AlN film surface morphology. Image processing was necessary in some cases to remove instrument artifacts such as scan lines. Visual determination of film morphology provides a reasonable estimate of film zone type based on selection criteria in the literature.[65] Z1 films comprise poorly crystalline or amorphous columns separated by voids; the columns may form conical structures that terminate in domes at the film surface. ZT films are also columnar, but lack large intercolumnar voids and domes.

AFM imagery of films taken from representative regions on the stress response surface provides compelling evidence for microstructural modification in low temperature reactive sputtered AlN films (Figure 15). ZT-like microstructure was observed for films sputtered at 1.9 kW and 2.15 mtorr, while films deposited at lower energies and higher pressures exhibit Z1-like microstructure. Film tensile stress increases with flux thermalization distances and reaches a maximum where microvoids are the dominant stress mechanism. Subsequent increases in the thermalization distance decreases film stress by increasing the intercrystallite void density.

Additional AFM film surface analysis involving axial points in the central composite designed experiment indicate that ZT-like film microstructure formation is promoted by decreased deposition pressure, increased deposition power (Figures 16a and 16d). A similar transition is seen for increased

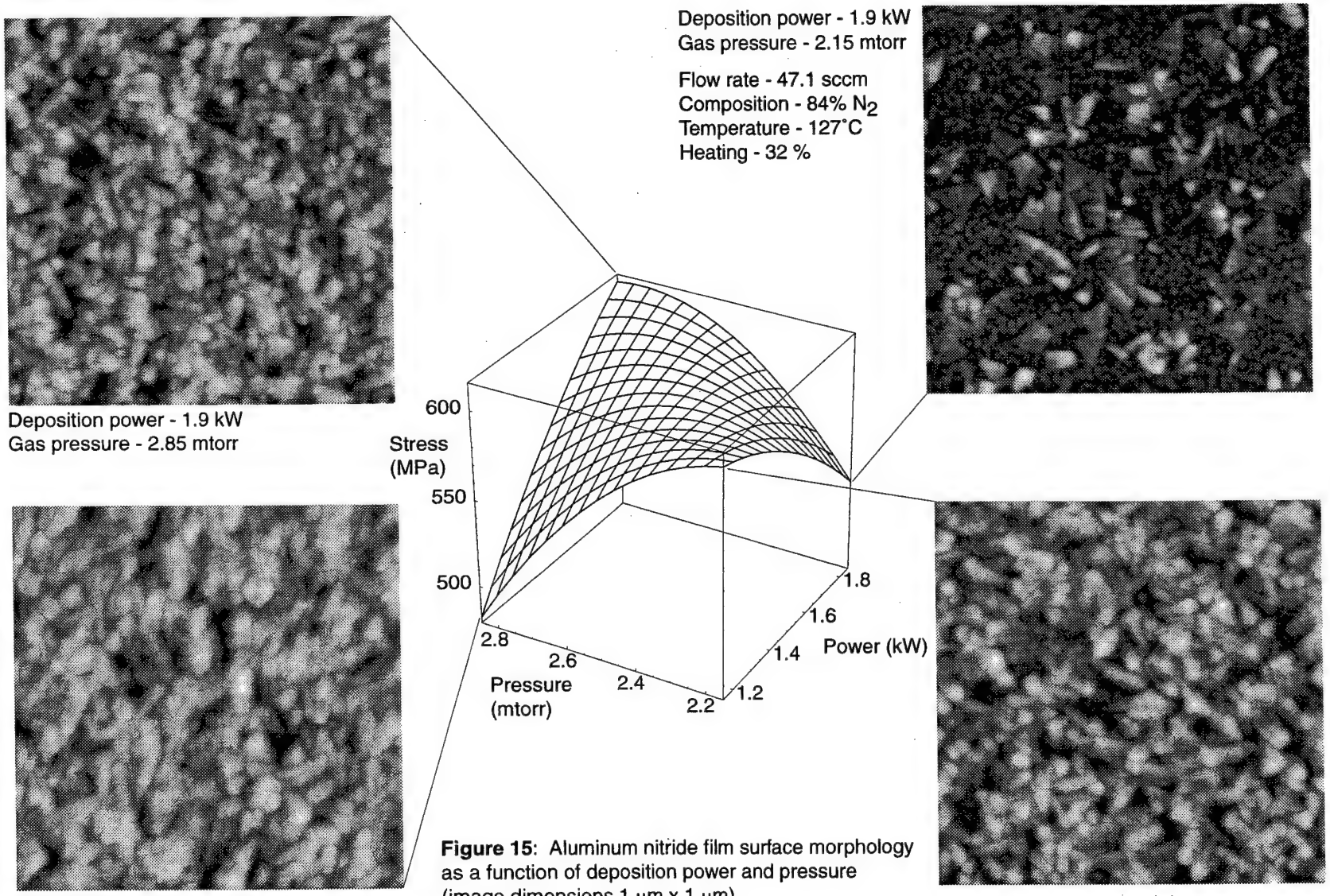


**Figure 15**: Aluminum nitride film surface morphology as a function of deposition power and pressure (image dimensions 1 μm x 1 μm)

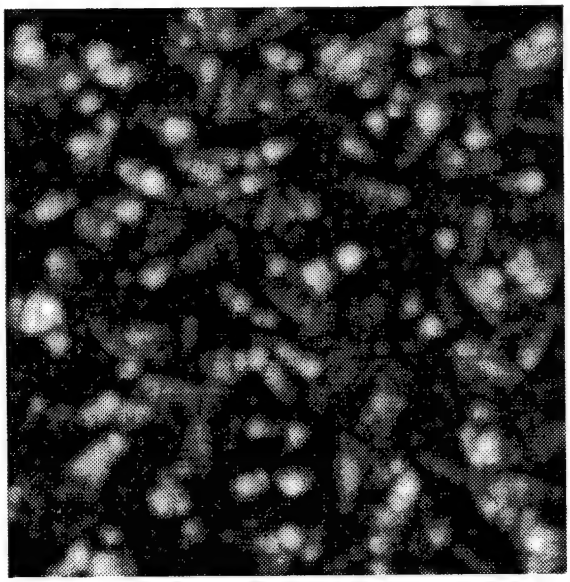

a) Deposition power - 2.5 kW

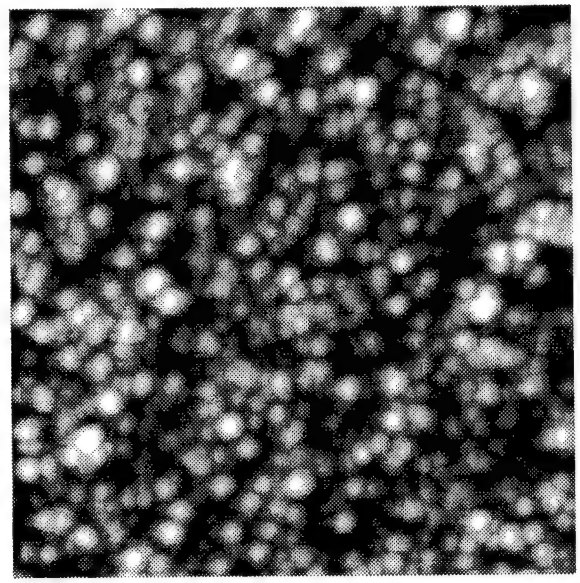

b) Deposition power - 0.5 kW

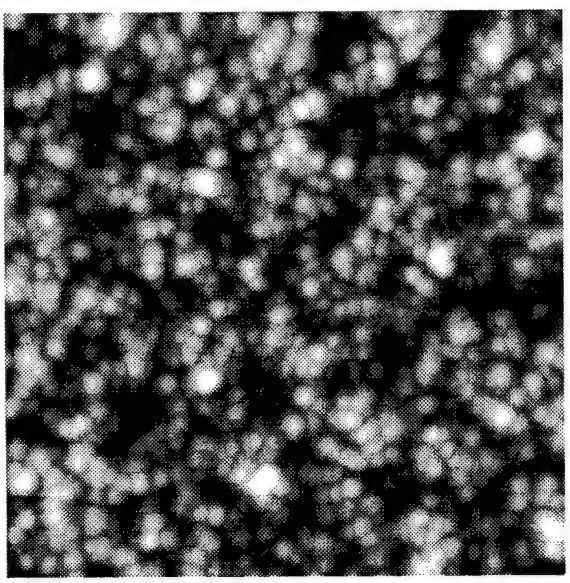

c) Gas pressure - 3.5 mtorr

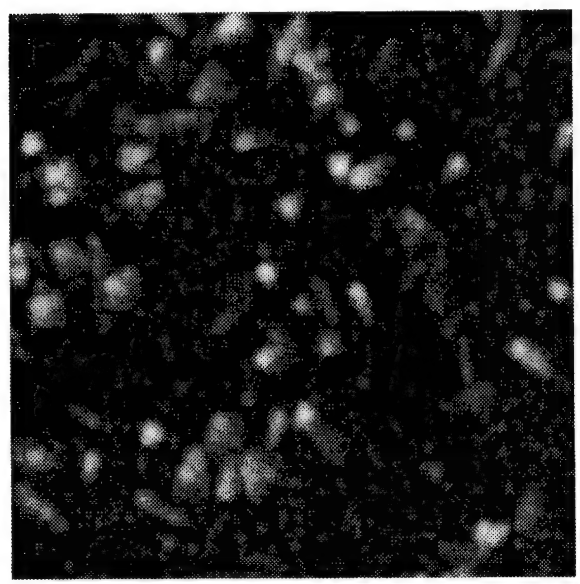

d) Gas pressure - 1.5 mtorr

**Figure 16**: Microstructural Zone Transitions due to Deposition Power and Pressure
(image dimensions 1 μm x 1 μm)

nitrogen concentration and to a lesser extent, increased initial substrate temperature. Remaining films are Z1 in nature, as seen in Figure 16b and 16c. The observations are in agreement with the film microstructure predicted by changes in film stress. Though ZT films have higher crystallinity than Z1 films, the transition does not undergo a maximum as is the case for film stress. Crystallinity by itself is not useful in predicting the film microstructure.

4.2.2 *Fracture morphology*

Fracture surface morphology was characterized via scanning electron microscopy. Because AlN is a dielectric material, a thin metal film is deposited on the fracture surface. The film is polycrystalline and textured, with columnar crystallites oriented normal to the substrate surface. The thickness of the film is in good agreement with values determined via spectroscopic ellipsometry. Surface morphology seen in the micrograph is consistent with the AFM findings discussed previously.

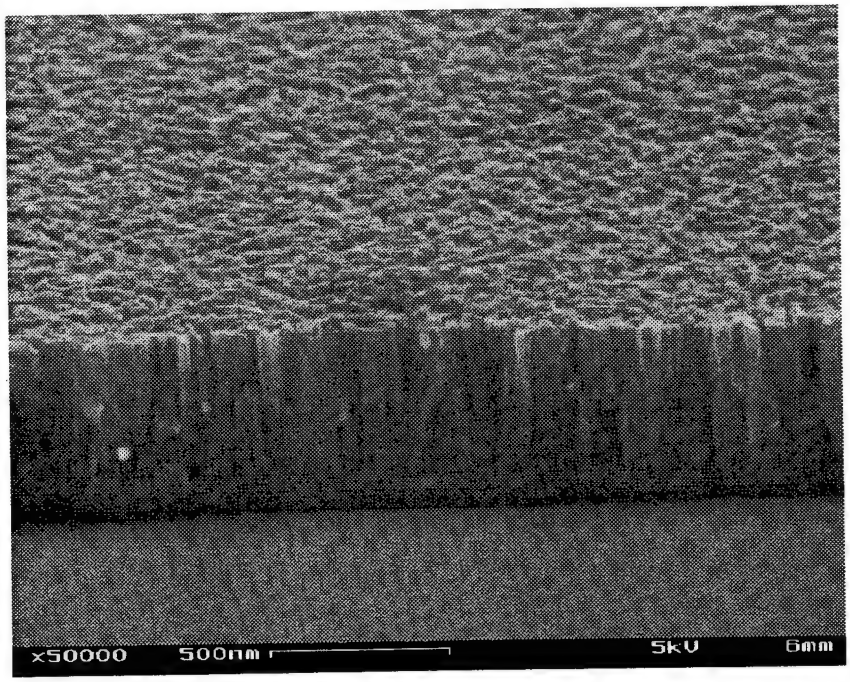


**Figure 17**: AlN Film Fracture Surface

4.2.3 *Adatom mobility*

The adatom mobility is affected by substrate temperature, roughness, and surface contaminants. The particle flux energy also contributes to adatom mobility. Quantitative determination of the mobility value is beyond the scope of this work. However, semi-quantitative data is available and may be of value in experimental design to determine the actual values. The following discussion assumes that the adatom diffusion length is on the same order of magnitude as the crystallite diameter.

Two sources of data can provide insights into the adatom mobility with the above conjecture. The AlN (0002) peak FWHM is indicative of the average crystallite size in the film

sample. The measurement is approximate, as instrument broadening effects affect the value. AFM micrographs can also be used to estimate crystallite size based on surface morphology. The technique is more applicable to ZT films than Z1 films, as several crystallites may be clustered within the Z1 dome structures.

XRD measurements are summarized below in Figure 18. The range of 25 to 45 nm is within a factor of two compared to the surface diffusion data presented in Table 2. AFM measurements indicate that the crystallite diameters range from 20 to 40 nm, which is consistent with the XRD results. The ZT films are more consistent in size compared to Z1 films, which vary widely. Larger surface features, on the order of 60 to 100 nm, are assumed to be domelike aggregates of crystallites that were unresolved by the tip.

The increase in crystallite size reflects heightened adatom mobility, given the assumption that the adatom diffusion length is on the same length scale as the crystallite size. Improved film crystallinity occurs with an increase in crystallite size and adatom mobility. Peak FWHM, indicative of film crystallinity, is improved by increasing the gas flow rate and substrate temperature. Increasing the flow rate affects the oxygen residence time by helping to sweep outgassed contaminants into the cryo pump. Oxygen binds strongly to aluminum and decreases the overall adatom mobility. Increasing the substrate temperature imparts greater energy to the adatoms and improves their mobility on the substrate surface.

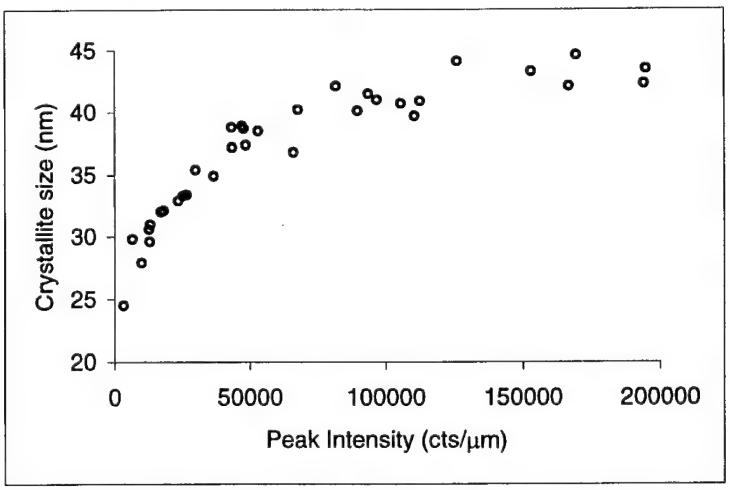


**Figure 18**: Film Crystallite Size and X-ray Peak Intensity

## 4.3 Roughness

Surface roughness of the substrate and film are important considerations in device fabrication. Substrate surface roughness affects resultant film properties, and the newly deposited film itself may serve as the substrate for subsequent processing. Initially, device wafer surfaces were assumed to be the same as the test wafers used in this study. Changes in processing upstream from the AlN deposition step forced a reassessment of the assumption. Increased substrate roughness was found to severely degrade film crystallinity, resulting in nonfunctional devices. The problem was addressed by adjusting the deposition conditions to improve adatom mobility to overcome the surface roughness. Surface roughness of the film may present similar consideration for further processing, and should also be taken into consideration.

### 4.3.1 *Substrate*

Experimental data was used throughout the study to optimize sputtering conditions for MEMS chemical sensor device wafers. However, the optimized conditions failed to yield predicted film crystallinity in devices fabricated using revised processing conditions. Silicon membranes used in the sensors were originally fabricated with a diffused boron etch stop process which left the substrate surface unaffected for AlN deposition. Device fabrication of the new devices involved removal of thermal oxide from the substrate surface. Oxide etching increases substrate surface roughness due to the nonabrupt nature of the Si-$SiO_2$ interface.[66] The increased substrate surface roughness probably degrades film crystallinity by impeding adatom mobility during film nucleation and growth.[41] Decreased adatom mobility due to oxygen contamination and lower substrate temperature were both factors that contributed to degradation in crystallinity in this study. The increased substrate surface roughness is likely to be a contributory factor in decreasing AlN film crystallinity and piezoelectric response.

AFM was used to characterize and quantify differences between the etched and untreated Si substrates. A $3^2$ factorial experiment involving three variables was used to assess the effect of substrate roughness and plasma power on crystallinity. The increased plasma power attempts to vary the adatom energy and flux to overcome the substrate surface roughness; films were deposited at 1.0 kW and 2.5 kW constant power. As the MEMS device wafers were costly to prepare, only two were available for experimentation. 1-$cm^2$ fragments were cut from an untreated *p*-type Si wafer and one of the device wafers with a die saw to

increase the number of samples available for experimentation. The third variable, sample type, categorically accounts for differences between fragments and whole wafers. The use of wafer fragments permits concurrent deposition on both substrate types, thereby allowing for direct comparisons to be made between the resultant film crystallinity without regard to variation between depositions.

AFM measurements indicate that the untreated Si surface has a root-mean-square (RMS) surface roughness of 0.151 nm; the oxide etched surface, 0.526 nm. These values agree with values previously reported in the literature.[66] XRD rocking curve data was analyzed with regards to substrate surface roughness, plasma power, and sample type. The FWHM values can be described via equation (14) for whole wafers and (15) for wafer fragments:

$$\text{FWHM} = 3.11 + 1.98\ (\textbf{Surface roughness}, \text{nm}) - 0.12\ (\textbf{Power}, \text{kW}) \quad (14)$$

$$\text{FWHM} = 3.09 + 7.75\ (\textbf{Surface roughness}) - 0.12\ (\textbf{Power}) \quad (15)$$

The electromechanical coupling coefficient for AlN remains constant with regard to the FWHM value up to 3°. The piezoelectric response has been observed to drop off sharply when the FWHM value exceeds 3°.[53] The increase in surface roughness and concomitant drop in film crystallinity is a contributory factor in device failure where oxide-etched silicon substrates were used. The experimental evidence suggests that process-induced roughening of substrate surfaces can be a significant factor in degrading piezoelectric response in sputtered thin films at low substrate temperatures. The decrease in film crystallinity for films deposited on wafer fragments suggests that the proximity of the substrate edge also has a role in determining film crystallinity.

4.3.2 *Growth*

Final film RMS roughness range between 2.5-5.8 nm, significantly higher than the initial substrate roughness. ZT films, seen in Figure 16a and 16d, typically have lower roughness compared with Z1 films. Interestingly, films deposited in pure $N_2$ have high surface roughness despite having underlying ZT microstructure (Figure 19). This is likely due to the development of Z1 protuberances from the film surface as the surface morphology transitions between ZT and Z1. All ZT films exhibit these surface features to an extent. The difference in height between the protuberance and the smoother underlying ZT microstructure leads to greater surface roughness than Z1 films, where the domelike surface structures abut and overlap.

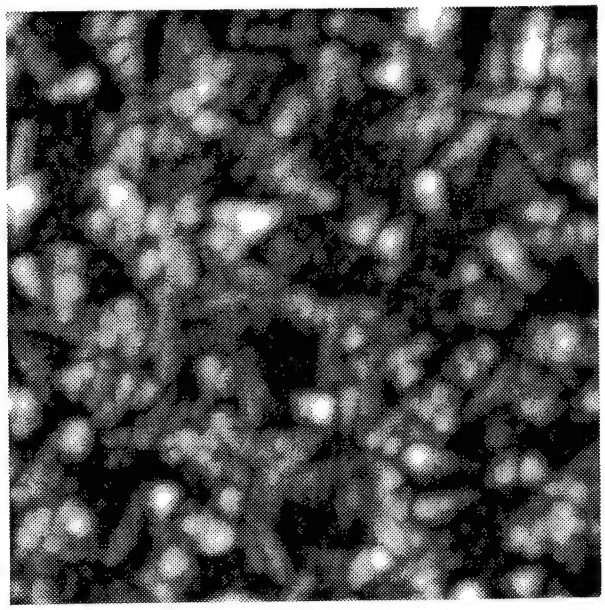

**Figure 19**: Z1-ZT Transitional Film Surface
1.5 kW, 2.5 mtorr, 40 sccm, 100% $N_2$, 100°C, 50% heating
Image dimensions 1 μm × 1 μm

4.4 Composition

Film composition is measured via x-ray photoelectron spectroscopy (XPS). Argon sputtering of the film surface is used to perform depth profiling. The sputtering rate is very low, typically 17Å/min, and the ion gun is used primarily to remove surface contaminants. The AlN films appear to be stoichiometric. Carbon contamination occurs only on the film surface, and is not found in the bulk of the film. For reasons discussed previously, the film oxygen content is inversely proportional to the gas flow rate, 5.53 atomic percent at 20 sccm and 3.79 atomic percent at 60 sccm. Film crystallinity is proportional to the flow rate and inversely proportional to the oxygen content, where the rocking curve FWHM is 4.46° at 20 sccm and 3.46° at 60 sccm.

Compositional analysis is complicated by the difficulty of consistency in the operation of the XPS equipment. The high degree of affinity between aluminum and oxygen results in immediate recontamination of the Ar ion sputtered AlN surface by oxygen present in the XPS chamber. Consistent positioning of the sample under the analyzer and Ar ion gun also prove problematic. For these reasons, only a limited subset of the films were analyzed under XPS. A standard of known composition would be of great value in future XPS work with AlN film characterization.

## 5. CONCLUSION

Low stress piezoelectric AlN thin films were deposited for MEMS device application using DC magnetron reactive sputtering. Film microstructure and properties were found to vary as functions of deposition power and pressure, process parameters which affect impinging particle flux energy and adatom mobility. Transition from the voided and poorly crystalline zone 1 microstructure to the densely packed zone T microstructure occurs with energy enhancement and particle bombardment. Adatom mobility is affected by substrate temperature and surface contaminants. Control of the oxygen partial pressure is crucial in obtaining piezoelectric AlN films, as oxygen at the growing film surface drastically reduces adatom mobility and promotes amorphous film structures. Further film stress reduction may be achieved by increasing the ion peening of the growing film to increase the compressive stress component. Alteration of deposition parameters affecting particle flux energy and adatom mobility permits processing control over film crystallinity and stress. The ZT microstructure is preferable for device application. Film crystallinity and stress were optimized for device application using response surface methodology and a six-factor central composite designed experiment.

Control over film uniformity was not achieved in this work. Thickness uniformity appeared to be process parameter independent and not amenable to alteration. Device wafer mapping to determine piezoelectric uniformity proved unsuccessful due to postdeposition processing and differences in device layout on the wafer. However, it is important to note that both operational and failed devices were present on wafers where highly crystalline films were deposited. The cause for failure in these devices was not ascertained.

X-ray diffractometry is useful in discerning the film crystallinity, which provides information on the piezoelectric quality of the film. Though x-ray diffraction is a nondestructive means of analysis, the need to cut the wafer into samples precluded its use for device wafers in this work. The same consideration applied to the use of scanning electron microscopy, which requires an additional metallization step for imaging. Stress measurements and surface characterization via atomic force microscopy may provide a means to assess the film microstructure without damaging the wafer. Spectroscopic ellipsometry proved to be useful for measuring film thickness and index of refraction. X-ray photoelectron spectroscopy proved to be of limited use due to oxygen recontamination of the film surface.

## 6. FUTURE WORK

AlN is a promising material for integrating MEMS technology with CMOS circuits. Its piezoelectric coupling coefficient is comparable to ZnO, which has found use with MEMS devices. Moreover, AlN is used in conjunction with GaN for optoelectronic applications, presenting the possibility of implementing multiple functionality on the same device using a single film layer. However, a number of processing issues remain to be resolved before this can be realized.

The role of oxygen in degradation of film piezoelectric response should be clarified. While oxygen does appear to degrade adatom mobility, other mechanisms may also be at work. The relatively high oxygen content measured by XPS is assumed to be due to oxygen recontamination of the sputtered film surface. AlN is known to form oxygen-containing polytypoids and inversion domain boundaries when the oxygen content in the lattice reaches a critical value. Inversion domain boundaries and oxygen-induced defects within crystalline grains have been observed in bulk studies with sintered AlN. Transmission electron microscopy of sputtered AlN thin films should be undertaken to determine if inversion domain boundaries play a role in degrading piezoelectric response. Regardless, an improved characterization of the individual crystallites within the film will be of value in understanding the piezoelectric response of the material.

Improvement of film thickness, composition, and microstructural uniformity serve to increase device performance uniformity. However, as the thickness uniformity is unresponsive to process parameter changes, hardware modifications in the target, substrate, and gas flow geometry may be necessary to produce changes. Substrate rotation is a possible avenue of investigation in improving film uniformity. Another approach is to implement substrate biasing to increase the resputtering of the growing film surface.

An enhanced understanding of AlN processing requirements is of value for MEMS application, particularly with regard to potential on-chip integration with microelectronic circuits and other system components. The microstructural transition and region of optimal film property identified in this work highlight the potential benefits offered by further characterization of AlN processing and properties.

APPENDIX 1: Data Summary

| Run | Pwr | Psr | FIR | Comp | Tmp | Heat | Time | Intensity | Rocking | PrSt | FlStr | Uniform | Rough |
|---|---|---|---|---|---|---|---|---|---|---|---|---|---|
| 042 | 1.5 | 2.5 | 40 | 75% | 102 | 50% | 20 | 15591 | 4.697 | 657 | | 10.93% | |
| 043 | 1.5 | 2.5 | 40 | 75% | 104.8 | 50% | 20 | 31718 | 3.765 | 713 | | 11.25% | |
| 044 | 1.0 | 1.7 | 40 | 75% | 100.7 | 20% | 20 | 140547 | 3.451 | 512 | | | |
| 045 | 1.5 | 2.5 | 40 | 75% | 99.1 | 50% | 17 | 51936 | 4.012 | 651 | | 11.05% | |
| 046 | 1.5 | 2.5 | 60 | 75% | 99.9 | 50% | 17 | 78120 | 3.636 | 659 | | 11.41% | |
| 047 | 1.5 | 2.5 | 40 | 75% | 101.8 | 0% | 17 | 32300 | 4.048 | 699 | | 11.28% | |
| 048 | 1.5 | 2.5 | 40 | 100% | 106.5 | 50% | 17 | 137150 | 3.1685 | 589 | | 10.84% | |
| 049 | 1.5 | 2.5 | 40 | 75% | 99.8 | 50% | 17 | 39037 | 4.109 | 618 | | 11.03% | |
| 050 | 1.5 | 3.5 | 40 | 75% | 101.5 | 50% | 18 | 6201 | 5.293 | 498 | | 11.12% | |
| 051 | 1.5 | 2.5 | 20 | 75% | 100.3 | 50% | 17 | 21612 | 4.599 | 629 | | 11.25% | |
| 052 | 1.5 | 2.5 | 40 | 75% | 175 | 50% | 17 | 3215 | 6.458 | 653 | | | |
| 053 | 1.5 | 2.51 | 40 | 75% | 24.8 | 50% | 17.2 | 5323 | 6.662 | 652 | | | |
| 054 | 1.5 | 2.5 | 40 | 75% | 103 | 50% | 17 | 16867 | 5.092 | | | | |
| 055 | 1.0 | 1.5 | 60 | 100% | 115 | 20% | 30 | 287192 | 2.862 | 229 | | | |
| 056 | 1.5 | 2.5 | 40 | 75% | 100.7 | 50% | 17 | 1911 | 6.52 | 677 | | | |
| 057 | 1.5 | 2.5 | 40 | 75% | 100.4 | 50% | 17 | 2080 | | 638 | | 11.08% | |
| 058 | 1.5 | 2.5 | 40 | 75% | 109.3 | 50% | 17 | 28443 | 3.776 | 658 | 488 | 10.40% | |
| 059 | 1.5 | 2.49 | 40 | 75% | 104.3 | 0% | 17 | 19287 | 4.113 | 602 | 407 | 8.57% | 5.249 |
| 060 | 2.5 | 2.5 | 40 | 75% | 100.9 | 50% | 9 | 166211 | 3.402 | 630 | 612 | 11.57% | 3.845 |
| 061 | 1.5 | 1.5 | 40 | 75% | 100.8 | 50% | 17 | 215771 | 3.306 | 447 | 263 | 10.82% | 2.482 |
| 062 | 1.5 | 2.5 | 40 | 50% | 102.1 | 50% | 17 | 11339 | 5.044 | 772 | 596 | 10.70% | 4.437 |
| 063 | 0.5 | 2.5 | 40 | 75% | 108.1 | 50% | 62 | 9978 | 4.861 | 494 | 131 | 10.86% | 4.658 |
| 064 | 1.5 | 2.5 | 40 | 75% | 106.7 | 50% | 17 | 80219 | 3.582 | 602 | 386 | 10.86% | |
| 065 | 1.5 | 2.5 | 40 | 100% | 100.2 | 50% | 17 | 170546 | 3.076 | 607 | 674 | 10.31% | 5.819 |
| 066 | 1.5 | 3.5 | 40 | 75% | 99.8 | 50% | 18 | 11959 | 4.686 | 401 | 194 | 11.38% | 4.695 |
| 067 | 1.5 | 2.5 | 40 | 75% | 103.1 | 100% | 13 | 49003 | 4.136 | 590 | 354 | 11.82% | 4.374 |
| 068 | 1.5 | 2.5 | 40 | 75% | 99.6 | 50% | 17 | 52312 | 3.929 | 715 | 633 | 11.70% | 3.695 |
| 069 | 1.5 | 2.5 | 60 | 75% | 115.9 | 50% | 17 | 88554 | 3.46 | 748 | 631 | 11.33% | 5.763 |
| 070 | 1.5 | 2.51 | 40 | 75% | 23.3 | 50% | 17 | 13711 | 5.02 | 605 | 498 | 11.83% | 4.563 |
| 071 | 1.5 | 2.5 | 20 | 75% | 102.4 | 50% | 17 | 27774 | 4.461 | | | | 4.687 |
| 072 | 1.5 | 2.5 | 40 | 75% | 171.9 | 50% | 17 | 53843 | 4.352 | 728 | 678 | 11.51% | 5.252 |
| 073 | 1.9 | 2.91 | 32.9 | 84% | 73.3 | 32% | 14 | 6078 | 6.947 | 455 | 469 | 9.13% | |
| 074 | 1.1 | 2.91 | 47.1 | 84% | 73.8 | 68% | 28 | 16961 | 4.969 | 432 | 252 | 11.51% | |
| 075 | 1.9 | 2.09 | 47.1 | 84% | 130.5 | 32% | 14 | 213403 | 3.313 | 485 | 415 | 11.69% | |
| 076 | 1.5 | 2.50 | 40.0 | 75% | 100.7 | 50% | 17 | 142854 | 3.387 | 652 | 506 | 11.76% | |
| 077 | 1.1 | 2.10 | 47.1 | 66% | 75.9 | 32% | 28 | 87150 | 3.742 | 618 | 580 | 12.10% | |
| 078 | 1.9 | 2.10 | 47.1 | 84% | 77.9 | 68% | 14 | 281439 | 3.179 | 516 | 524 | 11.80% | |
| 079 | 1.9 | 2.10 | 32.9 | 66% | 127.9 | 32% | 12 | 283887 | 3.346 | 535 | 451 | 11.61% | |
| 080 | 1.9 | 2.90 | 47.1 | 66% | 75.6 | 32% | 12 | 78756 | 3.981 | 558 | 311 | 11.75% | |
| 081 | 1.9 | 2.90 | 32.9 | 84% | 122.0 | 68% | 14 | 200504 | 3.134 | 659 | 490 | 11.92% | |
| 082 | 1.1 | 2.11 | 47.1 | 66% | 127.9 | 68% | 28 | 153716 | 3.334 | 625 | 530 | 11.07% | |
| 083 | 1.9 | 2.10 | 32.9 | 66% | 75.3 | 68% | 12 | 292609 | 3.271 | 553 | 456 | 11.66% | |
| 084 | 1.1 | 2.90 | 47.1 | 84% | 134.7 | 32% | 29 | 66338 | 3.556 | 424 | 276 | 12.10% | |
| 085 | 1.1 | 2.90 | 32.9 | 66% | 122.6 | 32% | 28 | 13548 | 4.845 | 410 | 321 | 12.00% | |

| Run | Pwr | Psr | FlR | Comp | Tmp | Heat | Time | Intensity | Rocking | PrSt | FlStr | Uniform | Rough |
|---|---|---|---|---|---|---|---|---|---|---|---|---|---|
| 086 | 1.1 | 2.90 | 32.9 | 66% | 76.1 | 68% | 28 | 38539 | 3.981 | 404 | 229 | 11.64% | |
| 087 | 1.1 | 2.10 | 32.9 | 84% | 121.2 | 68% | 29 | 351477 | 3.025 | 610 | 493 | 12.63% | |
| 088 | 1.5 | 2.50 | 40.0 | 75% | 101.1 | 50% | 17 | 181267 | 3.267 | 565 | 431 | 12.46% | |
| 089 | 1.9 | 2.90 | 47.1 | 66% | 125.6 | 68% | 12 | 53006 | 4.198 | 564 | 559 | 12.28% | |
| 090 | 1.1 | 2.10 | 32.9 | 84% | 73.5 | 32% | 29 | 44141 | 4.28 | 467 | 409 | 11.98% | |
| 091 | 1.5 | 2.50 | 40.0 | 75% | 99.5 | 50% | 17 | 100303 | 3.673 | 541 | 416 | 11.92% | |
| 092 | 1.1 | 2.10 | 32.9 | 66% | 125.4 | 32% | 28 | 76987 | 3.808 | 596 | 480 | 12.20% | |
| 093 | 1.5 | 2.50 | 40.0 | 75% | 102.9 | 50% | 17 | 55610 | 4.105 | 564 | 411 | 12.67% | |
| 094 | 1.9 | 2.10 | 32.9 | 84% | 122.5 | 68% | 14 | 296388 | 3.219 | 509 | 278 | 11.59% | |
| 095 | 1.9 | 2.85 | 47.1 | 84% | 75.3 | 68% | 15 | 34254 | 4.516 | 422 | 443 | 8.69% | |
| 096 | 1.9 | 2.85 | 47.1 | 84% | 126.5 | 32% | 15 | 91374 | 3.642 | 524 | 336 | 11.76% | |
| 097 | 1.1 | 2.85 | 47.1 | 66% | 126.7 | 68% | 24 | 28496 | 4.506 | 465 | 373 | 11.67% | |
| 098 | 1.1 | 2.85 | 47.1 | 66% | 73.8 | 32% | 24 | 7138 | 5.731 | 434 | 212 | 11.73% | |
| 099 | 1.9 | 2.15 | 47.1 | 66% | 73.2 | 32% | 13.47 | 220774 | 3.467 | 509 | 463 | 12.20% | |
| 100 | 1.1 | 2.15 | 32.9 | 66% | 73.1 | 68% | 23 | 57256 | 4.164 | 568 | 403 | 8.92% | |
| 101 | 1.1 | 2.85 | 32.9 | 84% | 124.7 | 68% | 23.5 | 43761 | 4.198 | 417 | 566 | 10.58% | |
| 102 | 1.9 | 2.15 | 47.1 | 66% | 125.2 | 68% | 16 | 180660 | 3.457 | 455 | 516 | 9.89% | |
| 103 | 1.1 | 2.15 | 47.1 | 84% | 75.3 | 68% | 26 | 100991 | 3.617 | 484 | 351 | 11.68% | |
| 104 | 1.1 | 2.85 | 32.9 | 84% | 74.5 | 32% | 24.25 | 22947 | 4.769 | 407 | 192 | 11.97% | |
| 105 | 1.9 | 2.85 | 32.9 | 66% | 74.2 | 68% | 13.8 | 25918 | 4.915 | 546 | 398 | 9.42% | |
| 106 | 1.1 | 2.15 | 47.1 | 84% | 126.4 | 32% | 24.8 | 151980 | 3.474 | 479 | 294 | 11.20% | |
| 107 | 1.9 | 2.87 | 32.9 | 66% | 126.8 | 32% | 13.4 | 59475 | 4.098 | 632 | 363 | 12.01% | |
| 108 | 1.9 | 2.13 | 32.9 | 84% | 71.7 | 32% | 14 | 222573 | 3.426 | 446 | 242 | 12.28% | |
| 109 | 1.9 | 2.15 | 47.1 | 84% | 126.8 | 68% | 14 | 338440 | 3.167 | 377 | 323 | 12.44% | |
| 110 | 1.9 | 2.85 | 32.9 | 84% | 73.5 | 68% | 15 | 82633 | 3.858 | 618 | 309 | 11.61% | |
| 111 | 1.9 | 2.86 | 47.1 | 66% | 73.9 | 68% | 13.8 | 25055 | 4.908 | 639 | 433 | 12.01% | |
| 112 | 1.1 | 2.85 | 32.9 | 66% | 127.5 | 68% | 24 | 14221 | 5.141 | 458 | 428 | 11.75% | |
| 113 | 1.9 | 2.15 | 32.9 | 66% | 75.1 | 32% | 14 | 121419 | 3.82 | 530 | 51 | 12.64% | |
| 114 | 1.9 | 2.16 | 47.1 | 84% | 74.1 | 32% | 14 | 386221 | 3.21 | 560 | 624 | 12.42% | |
| 115 | 1.1 | 2.85 | 47.1 | 84% | 73.0 | 32% | 24.25 | 121247 | 3.398 | 375 | 372 | 12.22% | |
| 116 | 1.1 | 2.85 | 47.1 | 66% | 127.0 | 32% | 23 | 84991 | 3.554 | 555 | 467 | 12.14% | |
| 117 | 1.5 | 2.50 | 40.0 | 75% | 102.1 | 50% | 17 | 221189 | 3.25 | 540 | 484 | 9.37% | |
| 118 | 1.1 | 2.85 | 47.1 | 84% | 127.1 | 68% | 24.25 | 188193 | 3.126 | 499 | 549 | 11.36% | |
| 119 | 1.9 | 2.85 | 47.1 | 66% | 127.3 | 32% | 14 | 172050 | 3.306 | 638 | 608 | 11.96% | |
| 120 | 1.1 | 2.15 | 32.9 | 84% | 126.8 | 32% | 26 | 347802 | 3.011 | 591 | 640 | 11.74% | |
| 121 | 1.5 | 2.50 | 40.0 | 75% | 100.0 | 50% | 17 | 270881 | 3.042 | 641 | 614 | 11.47% | |
| 122 | 1.1 | 2.15 | 32.9 | 84% | 73.9 | 68% | 26 | 386556 | 2.978 | 716 | 627 | 11.81% | |
| 123 | 1.1 | 2.15 | 47.1 | 66% | 74.6 | 68% | 23 | 204135 | 3.179 | 669 | 595 | 10.10% | |
| 124 | 1.1 | 2.85 | 32.9 | 66% | 73.8 | 32% | 24 | 52654 | 3.862 | 587 | 399 | 11.75% | |

Run – run number
Pwr – Deposition power (kW)
Psr – Gas pressure (mtorr)
FlR – Flow rate (sccm)
Comp – Composition (%$N_2$), remainder Ar
Tmp – Initial substrate temperature (°C)
Heat – Supplemental chamber heating (%)
Time – Deposition time (min)

Intensity – Normalized AlN (0002) peak intensity (counts/μm)
Rocking – Rocking curve FWHM (°)
PrSt – Profilometer stress (MPa)
FlStr – Flexus laser deflection stress (MPa)
Uniform – Uniformity (%)
Rough – Root-mean-square roughness (nm)

## APPENDIX 2: Residuals for response surface models

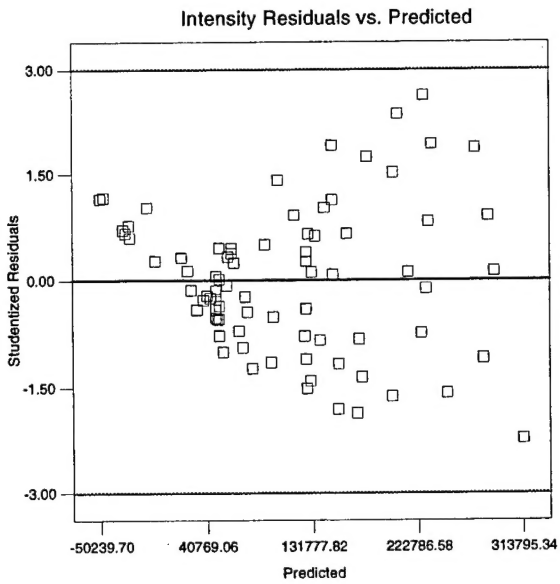


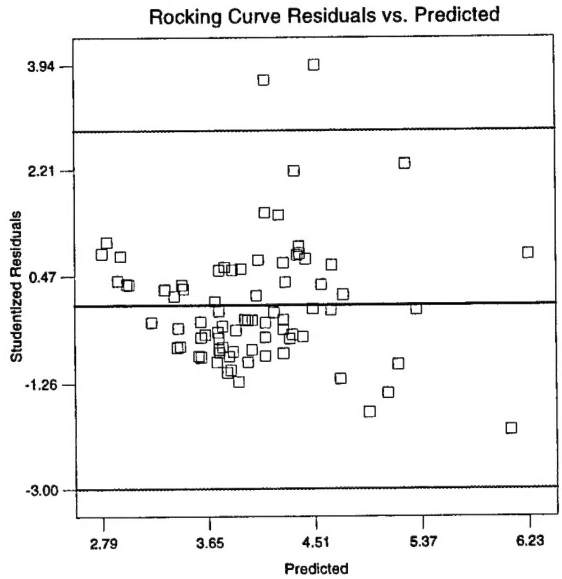


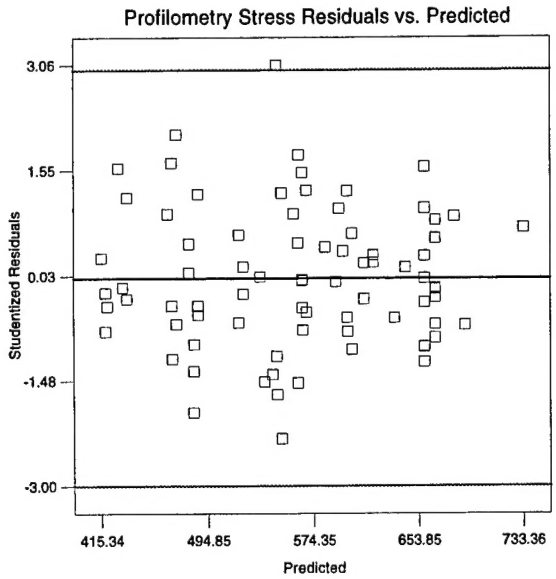


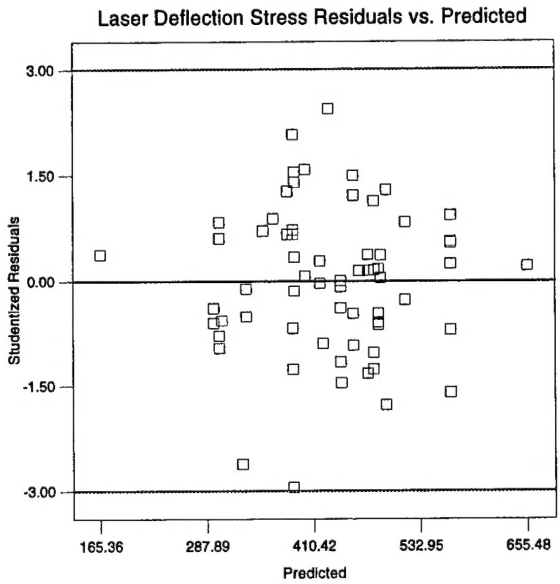

# APPENDIX 3: Standard error of response surfaces

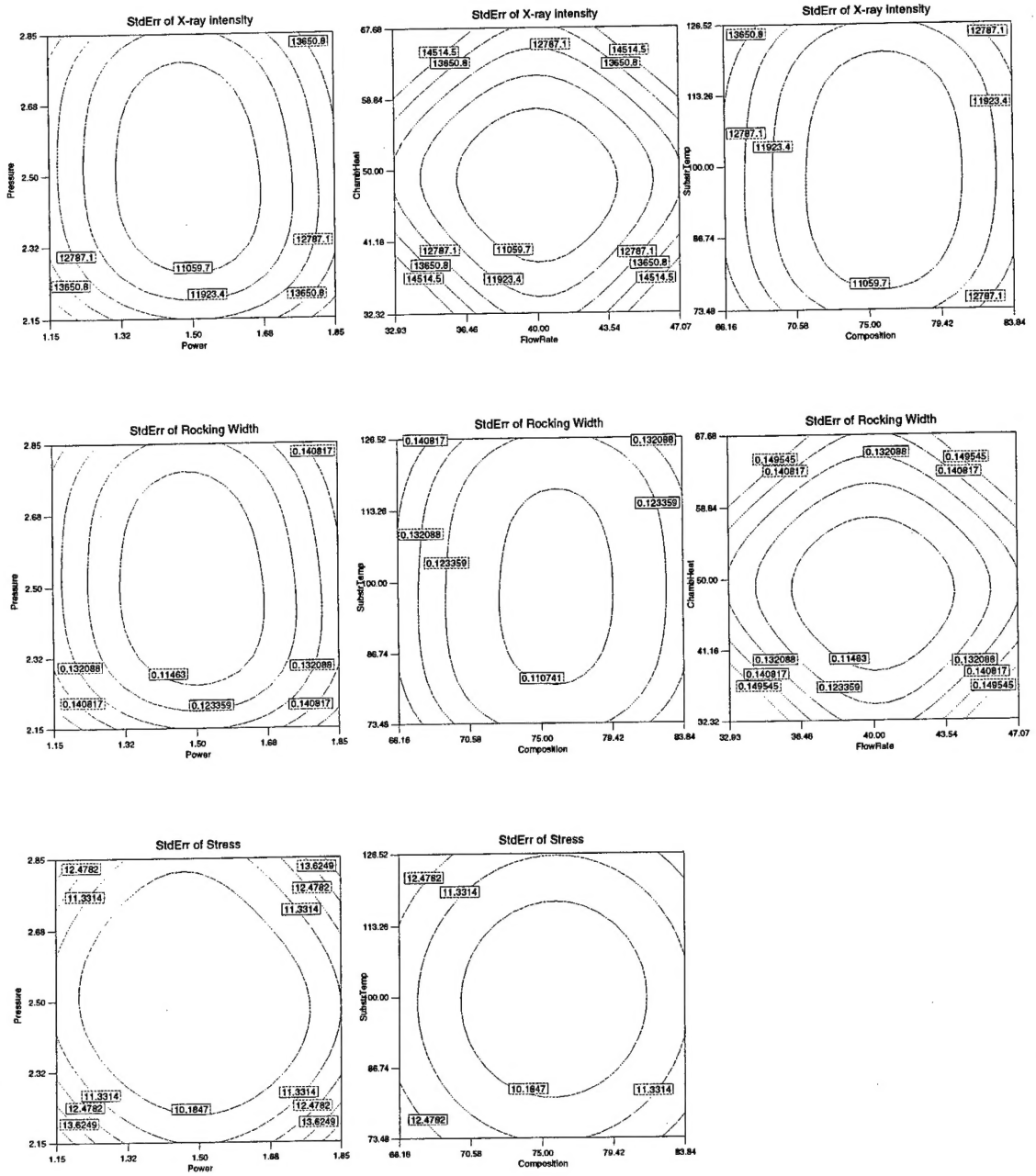

## BIBLIOGRAPHY


[1] A. Ballato, IEEE Trans. Ult. Ferro. Freq. Cont. **42** (5), 916 (1995).
[2] T. Ikeda, Fundamentals of Piezoelectricity, (Oxford University Press, New York, 1996) p. 209.
[3] P. Muralt, Integr. Ferro. **17**, 297 (1997).
[4] H. Ochs, D. Bublak, U. Wild, M. Muhler, and B.O. Kolbesen, Appl. Surf. Sci. **133**, 73 (1998)
[5] K. Chakrabarti, K.K. Chattopadhyay, S. Chaudhuri, and A.K. Pal, Mat. Chem. Phys. **50**, p. 50 (1997).
[6] *CRC Handbook of Chemistry and Physics,* edited by D.R. Lide (CRC Press, Ann Arbor, 1992), p. 12-83, 4-36.
[7] F. Ansart, H. Ganda, R. Saporte, J.P. Traverse, Thin Solid Films, **260**, 38 (1995).
[8] B. Chapman, *Glow Discharge Processes*, (John Wiley & Sons, New York, 1980), p. 180.
[9] J. Schulte, G. Sobe, Thin Solid Films, **324**, 19-24 (1998).
[10] R.F. Rutz, E.P. Harris, J.J. Cuomo, IBM J. Res. Develop **17**, 61 (1973).
[11] A.J. Shuskus, T.M. Reeder, E.L. Paradis, Appl. Phys. Lett. **24** (4), 155-156 (1974).
[12] T. Shiosaki, T. Yamamoto, T. Oda, A. Kawabata, Appl. Phys. Lett. **36** (8), 643-645 (1980).
[13] C.R. Aita, J. Appl. Phys. **53** (3), 1807-1808 (1982).
[14] F. Takeda, T. Mori, T. Takahashi, Jpn. J. Appl. Phys. **20** (3), L169-L172 (1981).
[15] J. Chaudhuri, R. Thokala, J.H. Edgar, B.S. Sywe, J. Appl. Phys. **77** (12), 6263-6266 (1995)
[16] S. Karmann, H.P.D. Schenk, U. Kaiser, A. Fissel, Wo. Richter, Mat. Sci. Engr. **B50**, 228-232 (1997)
[17] M. Katsikini, E.C. Paloura, T.S. Cheng, C.T. Foxon, J. Appl. Phys. **82** (3), 1166-1171 (1997)
[18] N. Tanaka, H. Okano, T. Usuki, K. Shibata, Jpn. J. Appl. Phys. Pt. 1, **33** (9B), 5249-5254 (1994)
[19] A. Kumar, H.L. Chan, J.J. Weimer, L. Sanderson, Thin Solid Films **308-309**, 406-409 (1997)
[20] M. He, N. Cheng, P. Zhou, H. Okabe, J.B. Halpern, J. Vac. Sci. Technol. A **16** (4), 2372-2375 (1998)
[21] R. Liu, in *ULSI Technology*, edited by C.Y. Chang and S.M. Sze (McGraw-Hill, New York, 1996) pp. 379-380.
[22] A. Bogaerts, R. Gijbels, Analytical Chemistry, **69** (23), 719A (1997).
[23] B. Chapman, in *Glow Discharge Processes*, (Wiley-Interscience, New York, 1980), p. 79.
[24] Ibid., 234.
[25] C.C. Fang, F. Jones, R.R. Kola, G.K. Celler, V. Prasad, J. Vac. Sci. Technol. B **11** (6), 2947-2952 (1993).
[26] W.D. Westwood, J. Vac. Sci. Technol. **15** (1), 1-9 (1978).
[27] D. Mahéo, J.-M. Poitevin, Thin Solid Films, **237**, 78-86 (1994).
[28] D.L. Smith, in *Thin-Film Deposition*, (McGraw-Hill, New York, 1995), pp. 445-446.
[29] G. Este, W.D. Westwood, J. Vac. Sci. Technol. A **5** (4), 1892-1897 (1987).
[30] S. Muhl, J.A. Zapien, J.M. Mendez, E. Andrade, J. Phys. D. Appl. Phys., **30** (15), 2147-2155 (1997).
[31] I. Petrov, A. Myers, J.E. Greene, J.R. Abelson, J. Vac. Sci. Technol. A **12** (5), 2846-2854 (1994).
[32] H.-C. Lee, Y.-J. Yong, J.-Y. Lee, Eur. J. Solid State Inorg. Chem. **31** (6), 513-523 (1994).
[33] W.J. Meng, G.L. Doll, J. Appl. Phys., **79** (3), 1788-1793 (1996).

[34] F.J. Hickernell, R.-X. Yue, F.S. Hickernell, IEEE Trans. Ultr. Ferro. Freq. Cont., **44** (3), 615-623 (1997)
[35] L. Zheng, S. Ramalingam, T. Shi, R.L. Peterson, J. Vac. Sci. Technol. A **11** (5), 2437-2446 (1993).
[36] K. Nomura, Y. Ishikawa, N. Shibata, Nippon Seram Kyo Gak, **102** (11), 1079-1081 (1994) [J. Ceram. Soc. Jpn. Int. Ed. **102** (11), 1083-1085 (1994)].
[37] B. Chapman, in *Glow Discharge Processes*, (Wiley-Interscience, New York, 1980), p. 203.
[38] D.L. Smith, in *Thin-Film Deposition*, (McGraw-Hill, New York, 1995), pp. 134-135.
[39] A.W. Adamson, A.P. Gast, in *Physical Chemistry of Surfaces*, 6th ed., (Wiley-Interscience, New York, 1997), pp. 648-649.
[40] *CRC Handbook of Chemistry and Physics,* edited by D.R. Lide (CRC Press, Ann Arbor, 1992), p. 9-129.
[41] J.A. Thornton, J. Vac. Sci. Technol. A **4** (6), 3059-3065 (1986).
[42] H.-C. Lee, J.-Y. Lee, H.-J. Ahn, Thin Solid Films **251**, 136-140 (1994).
[43] L.L. Levenson, A.B. Swartzlander, A. Yahashi, H. Usui, I. Yamada, Scanning Microscopy, **5** (3), 679-688 (1991)
[44] G. Carlotti, G. Gubbiotti, F.S. Hickernell, H.M. Liaw, G. Socino, Thin Solid Films, **310**, 34-38 (1997)
[45] D.L. Smith, in *Thin-Film Deposition*, (McGraw-Hill, New York, 1995), p. 143.
[46] W.J. Meng, J.A. Sell, G.L. Eesley, T.A. Perry, J. Appl. Phys, **74** (4), 2411-2414 (1993).
[47] J.-W. Soh, J.-H. Kim, W.-J. Lee, Jpn. J. Appl. Phys. Pt. 2, **35** (11B), L1518-L1520 (1996).
[48] S. Maniv, W.D. Westwood, J. Vac. Sci. Techol. **17** (3), 743-751 (1980).
[49] O.P. Karpenko, J.C. Bilello, S.M. Talisove, J. Appl. Phys., **82** (3), 1397-1403 (1997).
[50] K.H. Müller, J. Appl. Phys. **62** (5), 1796-1799 (1987).
[51] H.M. Liaw, W. Cronin, F.S. Hickernell, 1993 IEEE Ultrason. Symp. Proc., pp. 267-271.
[52] J.H. Harris, R.A. Youngman, R.G. Teller, J. Mater. Res., **5** (8), 1763-1773 (1990).
[53] R.S. Naik, PhD. Thesis, MIT, 1998
[54] T. Mattila, R.M. Nieminen, Phys. Rev. B **54** (23), 16676-16682 (1996).
[55] S. Maniv, W.D. Westwood, E. Colombini, J. Vac. Sci. Technol. **20** (2), 162-170 (1982).
[56] K. Kusaka, T. Hanabusa, K. Tominaga, Thin Solid Films **281-282,** 340-343 (1996).
[57] P. Jin, S. Maruno, Jpn. J. Appl. Phys. **30** (7), 1463-1468 (1991).
[58] H.-C. Lee, G.-H. Kim, S.-K. Hong, K.-Y. Lee, Y.-J. Yong, C.-H. Chun, J.-Y. Lee, Thin Solid Films **261**, 148-153 (1995).
[59] D.W. Hoffman, J.A. Thornton, J. Vac. Sci. Technol. **17** (1), 380-383 (1980).
[60] F.M. d'Heurle, Int. Mat. Rev. **34** (2), 53-68 (1989).
[61] E.P. Box, W.G. Hunter, J.S. Hunter, in *Statistics for Experimenters*, (Wiley, New York, 1978)
[62] R.S. Naik, MS Thesis, MIT, 1996.
[63] P.B. Legrand, M.Wautelet, B. Dugnoille, J.P. Dauchot, M. Hecq, Thin Solid Films, **248,** 220-223 (1994).
[64] D.L. Smith, in Thin-Film Deposition, (McGraw-Hill, New York, 1995), p.190
[65] Ibid., p. 160.
[66] C. Y. Chang and T. S. Chao, in *ULSI Technology*, C. Y. Chang and S. M. Sze (McGraw-Hill, New York, 1996) p. 76.